ADVANCED
ENERGY
MATERIALS
www.advenergymat.d

Hierarchical Polyelemental Nanoparticles as Bifunctional Catalysts for Oxygen Evolution and Reduction Reactions

Meiling Wu, Mingjin Cui, Lianping Wu, Sooyeon Hwang, Chunpeng Yang, Qinqin Xia, Geng Zhong, Haiyu Qiao, Wentao Gan, Xizheng Wang, Dylan Kline, Michael R. Zachariah, Dong Su, Teng Li, and Liangbing Hu**

Efficient electrocatalysts are critical in various clean energy conversion and storage systems. Polyelemental nanomaterials are attractive as multifunctional catalysts due to their wide compositions and synergistic properties. However, controlled synthesis of polyelemental nanomaterials is difficult due to their complex composition. Herein, a one-step synthetic strategy is presented to fabricate a hierarchical polyelemental nanomaterial, which contains ultrasmall precious metal nanoparticles (IrPt, ≈5 nm) anchored on spinel-structure transition metal oxide nanoparticles. The polyelemental nanoparticles serve as excellent bifunctional catalysts for the oxygen evolution reaction (OER) and oxygen reduction reaction (ORR). The mass catalytic activity of the polyelemental nanoparticles is 7-times higher than that of Pt in ORR and 28-times that of Ir in OER at the same overpotentials, demonstrating the high activity of the bifunctional electrocatalyst. This outstanding performance is attributed to the controlled multiple elemental composition, mixed chemical states, and large electroactive surface area. The hierarchical nanostructure and polyelemental design of these nanoparticles offer a general and powerful alternative material for catalysis, solar cells, and more.

1. Introduction

With growing energy demands and the depletion of fossil fuels, intense research has been conducted on renewable energy conversion and storage systems, such as fuel cells, metal–air batteries, and water electrolysis.[1–6] The oxygen electrode, which includes two reverse reactions, the oxygen reduction reaction (ORR) and oxygen evolution reaction (OER), is an essential component of many of these systems, particularly metal–air batteries.[7–9] However, the sluggish kinetics in the complex four-electron transfer process at the oxygen electrode results in the requirement of a large overpotential, impeding the efficiency of these reactions. Thus, an efficient bifunctional electrocatalyst is of paramount importance to decrease the ORR and OER overpotentials for practical application.

Single-composition catalysts typically show only selective OER or ORR activity due to specific affinity to the oxygen reaction intermediates ($^*O$, $^*OH$, $^*OOH$).[10] For example, Pt and its alloys are generally considered the most efficient ORR catalysts, but show low catalytic activity for OER.[11] Ir-based catalysts are the state-of-the-art OER catalysts, but are less active toward ORR.[12] According to the Sabatier principle, highly efficient oxygen reaction catalysts generally require interactions with the reaction intermediates that are neither too weak nor too strong.[1,10] Therefore, incorporating multiple active oxygen reaction catalysts with different bonding effects, such as Pt, Ir, and other non-precious materials (e.g., transition metal oxides), into a polyelemental catalyst is a desirable approach toward achieving bifunctional catalysts,[13,14] due to the optimized catalyst-reactant interactions for both OER and ORR.

Recently, tremendous efforts have been devoted to the synthesis of nanosized catalyst materials with various structures, such as alloyed, core-shell, hybrid, and porous morphologies, to improve the electroactivity of the catalyst.[15–19] Furthermore, polyelemental nanomaterials are proposed to minimize the precious metal usage and maximize the electroactive surface area.[14,20–23] However, preparing polyelemental nanocatalysts with an optimal structure is challenging due to the complex composition. The different atom

---

Dr. M. Wu, M. Cui, Dr. C. Yang, Q. Xia, G. Zhong, H. Qiao, W. Gan, Dr. X. Wang, Prof. L. Hu
Department of Materials Science and Engineering
University of Maryland
College Park, MD 20742, USA
E-mail: binghu@umd.edu
Dr. L. Wu, Prof. T. Li
Department of Mechanical Engineering
University of Maryland
College Park, MD 20742, USA
E-mail: lit@umd.edu
Dr. S. Hwang, Prof. D. Su
Center for Functional Nanomaterials
Brookhaven National Laboratory
Upton, NY 11973, USA
Dr. D. Kline
Department of Chemical and Biomolecular Engineering
University of Maryland
College Park, MD 20742, USA
Prof. M. R. Zachariah
Department of Chemical and Environmental Engineering
University of California
Riverside, CA 92521, USA

The ORCID identification number(s) for the author(s) of this article can be found under https://doi.org/10.1002/aenm.202001119.

DOI: 10.1002/aenm.202001119

sizes, crystal structures, miscibility, and other intrinsic properties of the components make it difficult to integrate diverse elements into a single polyelemental nanoparticle.[24] In traditional wet chemistry synthesis, polyelemental nanoparticles at thermodynamic phases often show low electroactive surface area and electrocatalytic activity.[25] On the other hand, high-entropy nanoparticles show homogeneous atomic mixing, but fail to concentrate the precious metals at the surface for optimal catalytically active surface area.[26,27] In addition, agglomeration of the nanocatalyst during voltage sweep can be a severe issue, resulting in poor stability.[28] As a result, it is necessary to develop stable polyelemental nanoparticles with optimized elemental mixing and structure in order to achieve effective bifunctional electrocatalysts for oxygen electrode reactions.

Herein, we present a facile one-step synthesis for hierarchical polyelemental nanoparticles (HPNPs) as an efficient bifunctional catalyst toward OER and ORR. We use a rapid, high-temperature pulse to instantly decompose a collection of metal precursors, containing 10 atom% precious metals (Pt and Ir) and 90 atom% transition metals (Fe, Co, and Ni), which subsequently solidify into polyelemental nanoparticles (**Figure 1**). Through the high-temperature treatment for 0.5 s in air, the transition metals form spinel-type transition metal oxide nanoparticles (FeCoNiO$_x$), while the precious metals form ultrasmall nanoparticles (IrPt, ≈5 nm in diameter) that are strongly anchored to the surface of the transition metal oxide nanoparticles, forming a hierarchical structure. This hierarchical nanostructure lowers the usage of precious metal, generates a large electroactive surface area, and stabilizes the IrPt alloy during the oxygen electrode reactions. Compared to other synthesis methods of metal-metal oxide materials with hierarchical structure, including chemical reduction,[29] solvothermal processes,[30] and sputtering methods,[31] the metal and metal oxide are simultaneously synthesized in a one-step process in a manner that is ultrafast, solvent/reductant-free, and easy to control. Different from previously reported multimetallic nanoparticles synthesized via thermal shock, which feature homogeneously mixed alloys,[26] the hierarchical structure demonstrated herein maximizes the electroactive surface area of the precious metal catalyst as well as the transition metal oxide nanoparticles for optimal OER and ORR bifunctional catalytic activity and nanocatalyst stability.

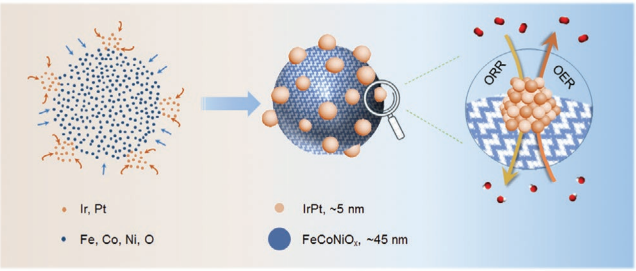

Figure 1. Schematic diagram of the one-step synthesis toward a hierarchical polyelemental nanostructure for use as a bifunctional catalyst in OER and ORR.

2. Results and Discussion

The synthesis begins by drop-casting metal precursors (nitrate and chloride salts) on a carbon substrate (carbonized wood, Figure S1, Supporting Information), featuring 10 atom% precious metals (Pt and Ir) and 90 atom% transition metals (Fe, Co, and Ni). The salt precursors have irregular shape and size and were randomly dispersed on the carbon substrate, as shown in the scanning electron microscopy (SEM) image in **Figure 2**a. A current pulse (3 A) is briefly applied for just 0.5 s through the precursor-loaded substrate in air to create a thermal pulse by Joule heating. The high-temperature treatment is indicated by a flash of light produced by the carbon substrate, which we used to calculate the temperature (≈1200 K) according to the blackbody radiation (Figure S2, Supporting Information).[32] The metal salts decomposed rapidly in one step and became nanoparticles uniformly distributed on the substrate (Figure 2b). The polyelemental nature of the uniformly distributed nanoparticles is indicated by the uniform energy-dispersive X-ray spectroscopy (EDS) elemental maps of Pt, Ir, Fe, Co, and Ni in Figure S3 in the Supporting Information. The mass content of the nanoparticles on the carbon substrate was ≈12.0 wt% (Figure S4, Supporting Information), corresponding to a mass loading of 4.7 mg cm^{-2}.

We demonstrate the hierarchical structure of the nanoparticles by scanning transmission electron microscopy (STEM), which shows ultrasmall nanoparticles dispersed on relatively larger nanoparticles (Figure 2c). From the high-angle annular dark-field (HAADF) STEM image in Figure 2d, we can see small particles with stronger contrast are anchored on larger nanoparticles with weaker contrast, and the corresponding EDS elemental maps (Figure 2d) clearly show that the smaller nanoparticles consist of Ir and Pt, and the larger nanoparticles consist of Fe, Co, Ni, and O. Thus, the large nanoparticles are composed of a transition metal oxide made of Fe, Co, and Ni (denoted as FeCoNiO$_x$) and the smaller nanoparticles are made of Ir and Pt (denoted as IrPt). Particle size analysis from SEM and STEM images shows that the average diameter of the FeCoNiO$_x$ nanoparticles was 44.4 ± 13.6 nm while that of the ultrasmall IrPt nanoparticles was only 4.7 ± 1.8 nm (Figure 2e). Therefore, a hierarchal polyelemental nanostructure with ultrasmall IrPt nanoparticles anchored on FeCoNiO$_x$ nanoparticles (denoted as FeCoNiO$_x$@IrPt) was obtained. This structure should result in a large electroactive area on the FeCoNiO$_x$ nanoparticle substrate, which is beneficial to catalytic activity.

We also performed high-resolution STEM to determine the crystal structure of the FeCoNiO$_x$@IrPt HPNPs. As shown in Figure 2f, the lattice spacing of the substrate nanoparticles was 0.481 nm, which corresponds to d_{111} of the cubic spinel structure of transition metal oxides. The lattice fringes on the ultrasmall particles are ascribed to the (101) and (100) planes of PtM (M = Fe, Co, Ni), indicating a thin layer of PtM is formed on the spinel FeCoNiO$_x$. In addition, as shown in Figure 2g, (111) planes were identified in the small IrPt nanoparticles. Thus, the IrPt nanoparticles are anchored on spinel-type FeCoNiO$_x$ nanoparticles through Pt-M intermetallic bonding at the interface. The strong covalent bond between the two kinds of nanoparticles prevents the detachment and agglomeration of the IrPt

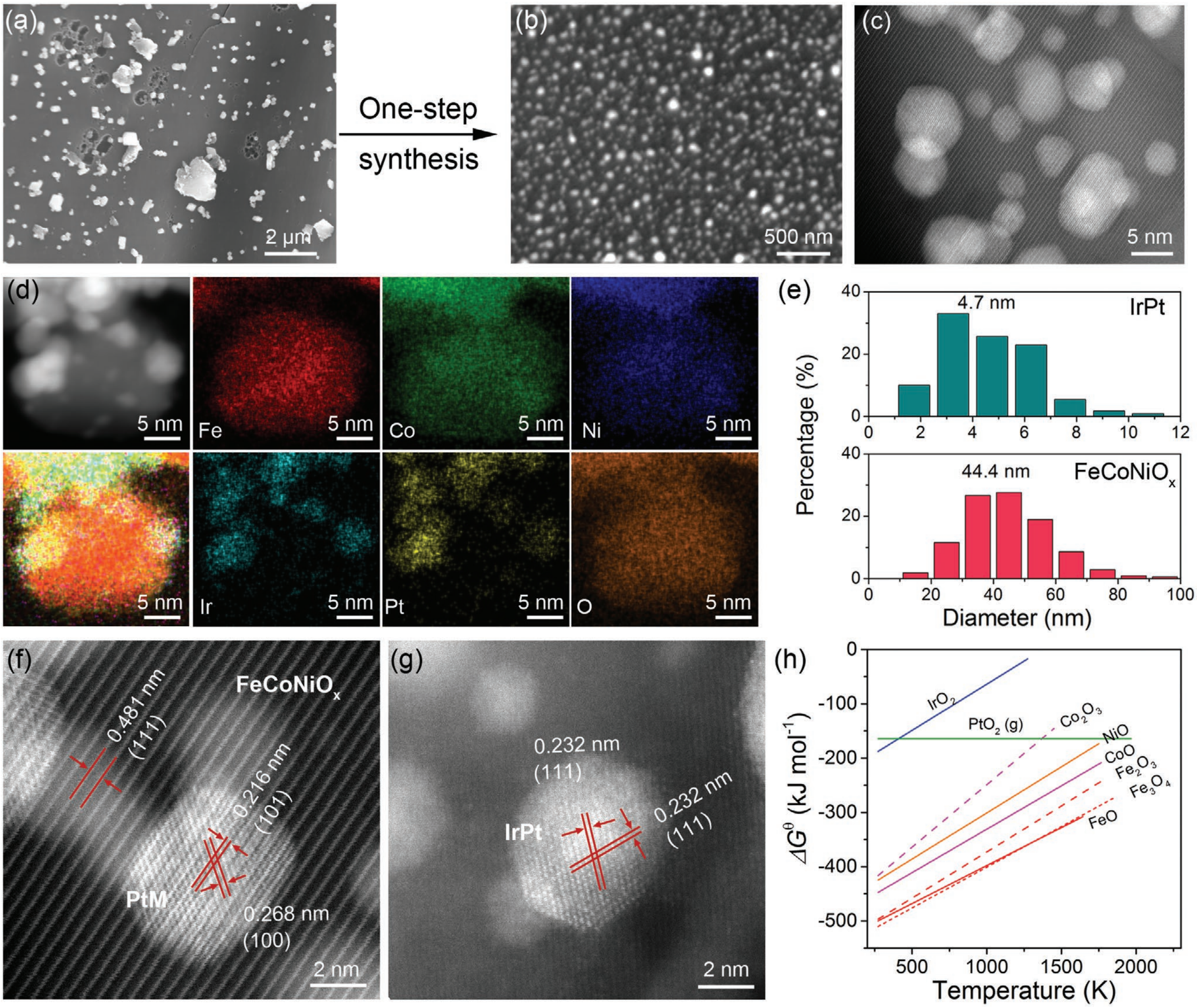

Figure 2. SEM images of a) precursor salts and b) the resulting nanoparticles on the carbon substrate, fabricated by the one-step, high-temperature shock technique. c) STEM image of the nanoparticles, demonstrating their hierarchical structure. d) HAADF-STEM image of a polyelemental nanoparticle and its corresponding EDS elemental maps. e) Size distribution of the (top) IrPt nanoparticles and (bottom) FeCoNiO$_x$ nanoparticles. f,g) Two typical high-resolution STEM images of the FeCoNiO$_x$@IrPt nanoparticles. The nanoparticles with bright contrast are ascribed to PtM or IrPt, under which is the FeCoNiO$_x$ with weaker contrast. The crystal planes of FeCoNiO$_x$, PtM and IrPt are indicated by red solid lines. h) The standard formation free energy of oxides from metal and oxygen as a function of temperature. Data calculated from ref. [34].

nanoparticles, which should enhance the structural stability of the nanocatalyst during electrochemical measurement.

According to the Ellingham diagram (Figure 2h), the free energy of formation (ΔG) of the transition metal oxides is more negative than that of the Ir and Pt noble metals at ≈1200 K, indicating that the transition metals are more inclined to form oxides in air atmosphere. Thus the transition metals (Fe, Co, and Ni) derived from the nitrate salt precursors were easily oxidized, whereas the Ir and Pt remained metallic as the high-temperature treatment was performed in air. To understand the formation of the hierarchical nanostructure, we synthesized FeCoNiO$_x$, Ir, and Pt nanoparticles using the same method. These simpler nanoparticles show a size distribution consistent with the polyelemental composite nanoparticles, in which the FeCoNiO$_x$ nanoparticles (47.8 ± 12.4 nm) are much larger compared to Ir and Pt (4.9 ± 1.3 nm and 1.9 ± 0.4 nm; Figures S5–S7, Supporting Information). As shown in Figure S8 in the Supporting Information, the vapor pressures of Fe, Co, and Ni are orders of magnitude higher than that of Ir and Pt. Thus the transition metals deposit slower during cooling after the high-temperature pulse and form larger nanoparticles than the precious metals. Entropy-driving force will facilitate the formation of the transition metal oxide mixture and IrPt alloy, respectively.[33] Thus, through this one-step synthesis, hierarchical polyelemental nanoparticles featuring different nanoparticle sizes were fabricated.

We performed X-ray diffraction (XRD) to further understand the crystal structure of the FeCoNiO$_x$@IrPt HPNPs.

As shown in **Figure 3**a, the peaks at 35.4°, 36.7°, 42.7°, 56.9°, and 62.0° are in agreement with the characteristic diffraction peaks of $CoFe_2O_4$, $NiFe_2O_4$, and CoO, which reveal the well-mixed spinel-type transition metal oxides of the $FeCoNiO_x$ nanoparticles. The obvious peaks at 41.4° and 47.6°, indicated by the blue-filled circles in Figure 3a, among a few other relatively weaker diffraction peaks are ascribed to the alloy of PtM, in good agreement with the STEM results. These crystal structures of PtM demonstrate the metallic bonds between M and Pt, which strongly anchor the IrPt nanoparticles on the $FeCoNiO_x$ substrate.[14] Raman spectroscopy was further applied to verify the lattice vibration from the transition metal oxide. As indicated in Figure 3b, the characteristic Raman peaks of FeO (A_{1g} at 323.3 cm^{-1}),[35] CoO (E_g at 479.1 cm^{-1}, F_{2g} at 622.5 cm^{-1}, and A_{1g} at 691.6 cm^{-1}),[36] Co_3O_4 (A_{1g} at ≈661.1 cm^{-1}),[37] and NiO (one-photon vibration at ≈567.6 cm^{-1})[38] further indicate the formation of mixed transmission metal oxides.

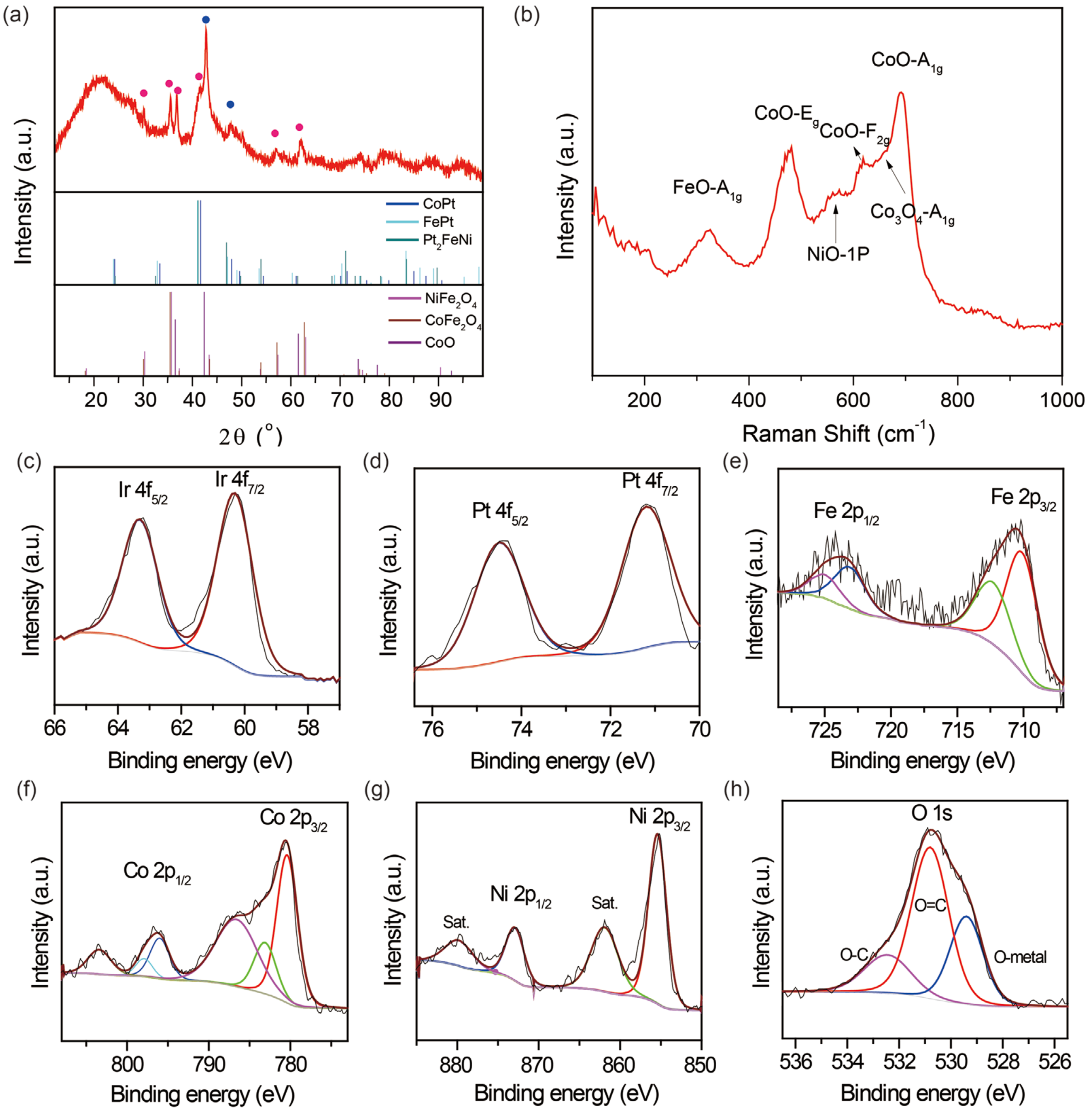

Figure 3. a) XRD pattern of (top) $FeCoNiO_x$@IrPt HPNPs. The standard XRD patterns of (middle) PtM and (bottom) transition metal oxide are derived from ICDD PDF card. b) Raman spectrum of the $FeCoNiO_x$@IrPt HPNPs. c–h) XPS spectra of c) Ir, d) Pt, e) Fe, f) Co, g) Ni, and h) O in the $FeCoNiO_x$@IrPt HPNPs.

We characterized the surface chemical states of the FeCoNiO$_x$@IrPt HPNPs by X-ray photoelectron spectroscopy (XPS) to further investigate the relationship between structure and electrochemical property. According to the XPS spectra, the Ir and Pt of the smaller nanoparticles are elemental metals (Figure 3c,d), which is consistent with their intrinsic inertness. In contrast, the transition metals show mixed valences in the polyelemental nanoparticles. As shown in Figure 3e, Fe showed a broad $2p_{3/2}$ peak with a binding energy at ≈710.5 eV, which can be attributed to a mixed state of FeO (710.2 eV) and Fe_2O_3 (712.6 eV). Co primarily exists as CoO ($2p_{3/2}$ peak at 780.5 eV) and a small portion of Co_2O_3 (783.2 eV), together with a satellite peak at 786.7 eV (Figure 3f). Similarly, Ni exists mainly as NiO with a $2p_{3/2}$ peak at 855.4 eV, along with a rather small fraction of Ni_2O_3 at 858.0 eV (Figure 3g). In addition, the O 1s peak at 529.2 eV (Figure 3h) originates from the transition metal oxide. This well-mixed FeCoNiO$_x$ containing different oxidization states (Fe^{2+}, Fe^{3+}, Co^{2+}, Co^{3+}, Ni^{2+}, and Ni^{3+}) will form a large amount of defects at the surface and change the electronic structure of the metal oxides,[39,40] which should benefit the oxygen catalysis activity. Furthermore, compared to single-element transition metal oxides, polyelemental transition metal oxides with mixed valences could further balance the adsorption and desorption energy between the intermediate oxygen and catalyst site,[10,39] significantly decreasing the ORR and OER overpotentials.

The polyelemental constituents of the HPNPs make them ideal catalysts for various electrocatalysis system. In particular, we were interested in demonstrating the bifunctional catalytic performances of the FeCoNiO$_x$@IrPt HPNPs for OER and ORR using the same electrode. To investigate the ORR and OER electrocatalytic activities, the synthesized HPNP catalysts were employed as the working electrode in 1 M KOH aqueous solution for both OER and ORR experiments. The carbon substrate of the polyelemental nanoparticles was used as a binder-free electrode substrate, which exhibited negligible OER activity by itself (Figure S9, Supporting Information). For comparison, FeCoNiO$_x$ nanoparticles (≈47.8 nm in diameter) and Ir nanoparticles (≈4.9 nm) synthesized using the same method were used as controls (Figures S5 and S6, Supporting Information).

As shown by the polarization curve obtained from linear sweep voltammetry (LSV, **Figure 4**a), the FeCoNiO$_x$@IrPt HPNP catalyst displays remarkably enhanced OER activity compared with the FeCoNiO$_x$ and Ir nanoparticles. The FeCoNiO$_x$@IrPt nanocatalyst shows a small overpotential of 240 mV at 10 mA cm^{-2}, which is much smaller than that of the FeCoNiO$_x$ (320 mV), Ir nanoparticles (280 mV), FeCoNiO$_x$@Pt (300 mV), and FeCoNiO$_x$@Ir (280 mV) prepared by the same method (Figure S11, Supporting Information). Containing only 5% of precious Ir in the polyelemental nanocatalyst, the overall mass activity for OER of FeCoNiO$_x$@IrPt was significantly improved compared to the transition metal oxide (FeCoNiO$_x$) and even the pure Ir catalyst (Figure S10, Supporting Information). The Tafel slope of FeCoNiO$_x$@IrPt (34 mV dec^{-1}) was also better than that of FeCoNiO$_x$ (83 mV dec^{-1}), approximating that of the pure Ir nanoparticles (59 mV dec^{-1}) (Figure 4b), which indicates the good OER kinetics of the polyelemental catalyst. Compared with other metal oxides,[41–43] the FeCoNiO$_x$@IrPt HPNP catalyst exhibits outstanding OER catalytic performance in terms of the small overpotential and low Tafel slope (Table S1,

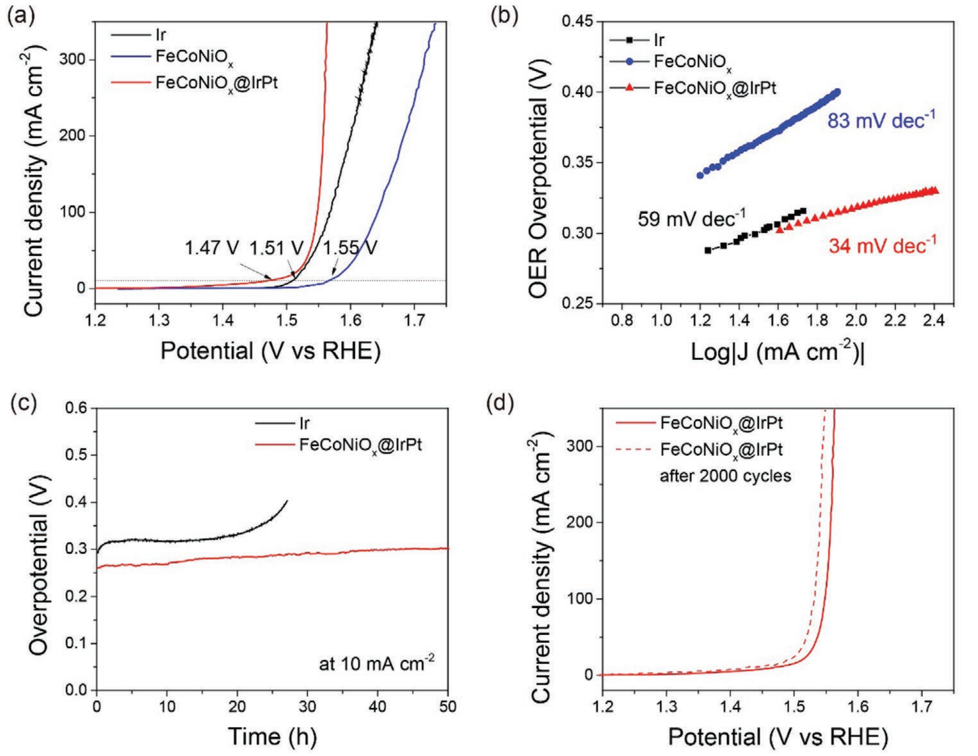

Figure 4. a) OER LSV curves and b) corresponding Tafel plots of FeCoNiO$_x$@IrPt, FeCoNiO$_x$, and Ir. c) OER chronoamperometry of FeCoNiO$_x$@IrPt and Ir at 10 mA cm^{-2} for 50 h. d) The LSV curves of FeCoNiO$_x$@IrPt before and after accelerated CV measurement at 50 mV s^{-1} for 2000 cycles.

Supporting Information), demonstrating the advantage of the hierarchical and polyelemental nanostructure.

We further examined the catalytic stability of the HPNP nanocatalyst by OER chronopotentiometry. The hierarchical FeCoNiO$_x$@IrPt shows a stable performance over 50 h at 10 mA cm^{-2}, with only a slight overpotential increase of 35 mV (Figure 4c), and a stable OER performance at high current densities up to 80 mA cm^{-2} for potential commercial applications (Figure S12, Supporting Information). In contrast, the OER overpotential of the Ir catalyst increased dramatically at 10 mA cm^{-2} after 20 h (Figure 4c). In addition, accelerated cyclic voltammetry (CV) was also employed to evaluate the stability of catalyst. After 2000 cycles at 50 mV s^{-1}, the LSV curve of FeCoNiO$_x$@IrPt shows minimal change from the initial LSV curve (Figure 4d), much more stable than the pure Ir (Figure S13, Supporting Information), indicating an excellent stability of the HPNPs for OER. However, the catalytic activity of Ir degenerated significantly under the same testing condition (Figure S13, Supporting Information). The morphology and particle size of the FeCoNiO$_x$@IrPt nanocatalyst also remained unchanged after the 50 h durability test, without particle agglomeration or detachment (Figure S14, Supporting Information), confirming the structural stability of the nanocatalyst over the long-term reaction. With IrPt content increased to 25% (atomic ratio, Ir:Pt = 1:1), the FeCoNiO$_x$@IrPt shows slightly lowered OER activity but maintains superb catalytic stability (Figure S15, Supporting Information).

To understand the high stability of polyemelemental FeCoNiO$_x$@IrPt, XPS was conducted on FeCoNiO$_x$@IrPt after OER stability test (accelerated CV). According to the XPS of Ir after OER (Figure S16, Supporting Information), the Ir was oxidized to IrO$_x$ on the surface of the HPNPs, which is the active site for OER in consistence with the previous literature.[44,45] Pt was also oxidized to high valences under high potential, indicated by the XPS in Figure S17 in the Supporting Information. The in situ formation of IrO$_x$ and mixed oxide of IrPtO$_x$ suppress the severe dissolution of Ir in alkaline solution and enhance the stability of FeCoNiO$_x$@IrPt.[46,47] In addition, the unique hierarchical nanostructure endows strong bonding between the FeCoNiO$_x$ nanoparticles and ultrasmall IrPt nanoparticles, with Pt-M intermetallic bonding for structural stability.

As a bifunctional oxygen electrocatalyst, we examined the performance of FeCoNiO$_x$@IrPt towards ORR by introducing saturated O$_2$ into the KOH electrolyte. FeCoNiO$_x$ and pure Pt nanoparticles were synthesized using the same method (Figure S7, Supporting Information) for controls. The LSV curve of the FeCoNiO$_x$@IrPt electrode (**Figure 5**a, red line) shows an onset potential of ORR at 0.93 V (vs RHE) and a half-wave potential ($E_{1/2}$) at 0.83 V (vs RHE), both of which outperform FeCoNiO$_x$. The Tafel slope of the FeCoNiO$_x$@IrPt HPNPs is 44 mV dec^{-1}, smaller than that of FeCoNiO$_x$ (52 mV dec^{-1}) and even less than that of Pt (63 mV dec^{-1}) (Figure 5b; Figure S18, Supporting Information), further confirming the fast catalytic ORR reaction kinetics of the polyelemental catalyst. Furthermore, as a bifunctional catalyst, FeCoNiO$_x$@IrPt shows high ORR catalytic activity when comparing its $E_{1/2}$ and Tafel slope with recently reported metal oxide catalysts for ORR (Table S2, Supporting Information).[48,49] Additionally, the $E_{1/2}$ of the HPNP catalyst only shifted negatively by ≈12 mV after 3000 cycles of accelerated cyclic voltammetry (CV) (conducted at 50 mV s^{-1}, Figure S19, Supporting Information), compared to the initial LSV curve, demonstrating the stability of FeCoNiO$_x$@IrPt over long-term ORR operation.

As discussed above, the HPNPs with ultrasmall IrPt nanoparticles at the surface increases the electroactive surface area of the catalyst. To further demonstrate this point, we measured the capacitance of FeCoNiO$_x$@IrPt to evaluate the electrochemical active surface area (ECSA) of the hierarchical nanoparticles for ORR. Based on the current density at different scan rates, the calculated double layer capacitance was 42.9 mF cm^{-2} (Figure S20, Supporting Information), indicating a large ECSA in the HPNP catalyst, producing abundant active sites for the electrocatalytic process. To determine the efficiency of the ORR reaction, we calculated the electron transfer number (n) according to the Koutecky–Levich equation based on the LSV curves at different electrode rotating speeds (Figure 4c).[50] The calculated n is ≈4.0, as shown in Figure 4d. Thus a nearly 4-electron reduction process of oxygen to water is obtained, which is critical for high efficiency in ORR. The full reaction of the OER and ORR performance of FeCoNiO$_x$@IrPt is displayed in Figure S21 in the Supporting Information as proof of its efficiency as a bifunctional oxygen catalyst.

The high activity of the bifunctional polyelemental catalyst is further shown in Figure 5e, in which we compared the mass activity of FeCoNiO$_x$@IrPt HPNPs (normalized to Ir or Pt) to that of pure Ir and Pt nanocatalysts in the OER and ORR, respectively. The OER mass activity of FeCoNiO$_x$@IrPt is ≈187 A g^{-1} Ir, which is a 28-times improvement compared to that of the pure Ir nanocatalyst (6.6 A g^{-1}), which is generally considered the state-of-the-art catalyst for OER. Moreover, the ORR mass activity of FeCoNiO$_x$@IrPt is ≈7.27 A g^{-1} Pt, which is ≈7-times the mass activity of the pure Pt nanocatalyst (1.08 A g^{-1}). The high mass activity of the FeCoNiO$_x$@IrPt nanoparticles reduces the use of precious metals while markedly promoting the bifunctional catalytic activity.

To understand the mechanism of the improved catalytic performance of the HPNP nanocatalyst, we conducted density functional theory (DFT) calculations in the ORR reactions catalyzed by FeNiCoO$_x$ and FeNiCoO$_x$@IrPt. The calculated energy diagrams of the ORR at 1.23 V for the different metal sites on two different structures (FeCoNiO$_4$ and FeCoNiO$_4$@IrPt) are calculated following the suggested reaction pathways (see detailed information in Experimental section). The limiting reaction barrier, which is determined from the free energy of the rate-determining step (RDS), is used to evaluate the catalytic activity. For the FeCoNiO$_4$ structure (Figure S22, Supporting Information), the limiting barriers of Fe, Co, Ni are 0.66, 1.24, and 0.61 eV, respectively. For the FeCoNiO$_4$@IrPt hierarchical polyelemental structure (Figure 5f), the limiting barriers of Fe, Co, Ni decrease to 0.62, 0.95, and 0.60 eV, respectively, and the Pt has a lower barrier of 0.49 eV. The lower limiting barrier for ORR indicates that the synergetic effect between FeCoNiO$_x$ and IrPt reduces the limiting reaction barrier of RDS on active sites and leads to the improved OER and ORR catalytic performance of FeCoNiO$_x$@IrPt. The bifunctional polyelemental catalyst with small overpotentials of OER and ORR will improve the energy efficiency of energy conversion and storage, particularly for metal–air batteries.

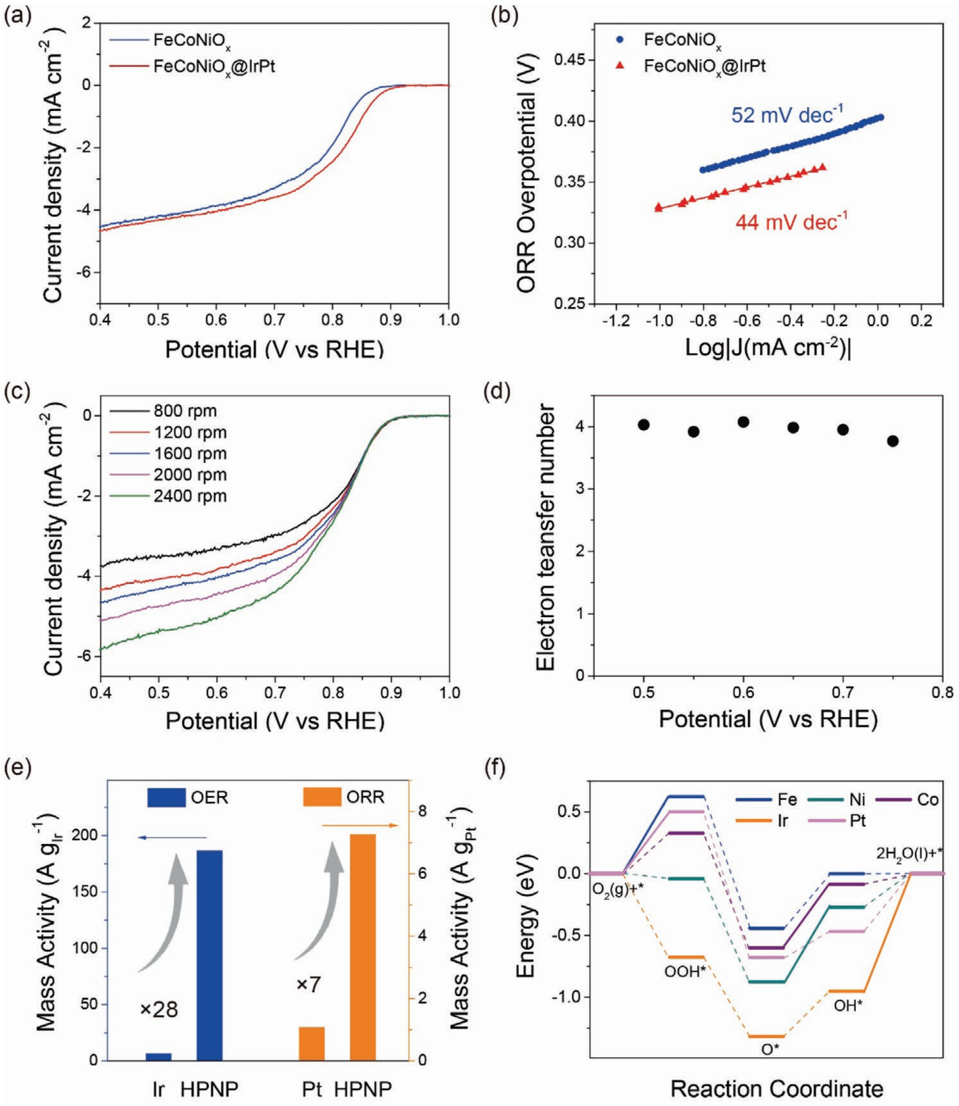

Figure 5. a) ORR LSV curves of FeCoNiO$_x$@IrPt and FeCoNiO$_x$. b) ORR Tafel plots derived from the LSV curves of FeCoNiO$_x$@IrPt and FeCoNiO$_x$. c) ORR LSV curves of FeCoNiO$_x$@IrPt at different rotating speeds. d) Electron transfer number as a function of the potential calculated from (c). e) Comparison of the mass activity of the FeCoNiO$_x$@IrPt HPNPs and noble metal controls: left, the OER mass activity (at an overpotential of 0.3 V) of FeCoNiO$_x$@IrPt versus Ir nanoparticles; right, ORR mass activity (at an overpotential of 0.4 V) of FeCoNiO$_x$@IrPt versus Pt nanoparticles. f) Free energy diagram at 1.23 V for ORR over Fe, Ni, Co, Pt, and Ir sites on the FeNiCoO$_x$@IrPt nanoparticle. The highlights indicate the rate-determining steps of the limiting energy barrier labeled.

3. Conclusion

We have presented a facile approach for the synthesis of hierarchical polyelemental bifunctional catalysts for efficient oxygen evolution and reduction reactions. Through a one-step synthesis, ultrasmall IrPt alloy nanoparticles were anchored on mixed spinel-type FeCoNiO$_x$ nanoparticles to produce a unique hierarchical catalyst. The nanocatalysts, which feature multiple active elements, mixed chemical states, and high electroactive surface area, exhibit synergistic and balanced adsorption/desorption properties that make them efficient bifunctional catalysts. These bifunctional nanocatalysts exhibit a small OER overpotential (240 mV) at 10 mA cm^{-2} and an ORR half-wave potential at 0.83 V (vs RHE). The mass activity of the polyelemental nanocatalyst (normalized to Ir or Pt) was 28-times compared to Ir in OER and 7-times compared to Pt in ORR under the same overpotentials. The high-temperature shock also enables Pt-metal bonding in the hierarchical nanoparticles, which provides a stable structure for durable electrocatalysis. This efficient and durable bifunctional oxygen electrocatalyst could greatly improve the energy efficiency of metal–air batteries and offer potential use in water electrolysis, fuel cells, and more. This hierarchical and polyelemental nanoparticle design opens a door for the discovery of other polyelemental nanomaterials for multifunctional catalysis featuring both long lifetime and cost efficiency.

4. Experimental Section

Preparation of the Carbon Substrate: The carbon substrate was made of carbonized wood. To make this support, basswood from Walnut Hollow Company was cut perpendicular to the tree growth direction into slices with thicknesses of ≈0.5 cm. The wood slices were first treated in air flow at 260 °C for 6 h, then annealed at 1000 °C in argon flow for another 6 h. The carbonized wood was further activated under CO_2 at 750 °C for 3 h, with a heating rate of 5 °C min^{-1}.

Fabrication of Electrocatalysts on Carbon Support: A mixed solution of $IrCl_3$, H_2PtCl_6, $Fe(NO_3)_3$, $Co(NO_3)_2$, and $Ni(NO_3)_2$ with a total metal ion concentration of 0.05 mol L^{-1} (metal ion ratio 5:5:30:30:30) in ethanol was first prepared. All the metal salts were used directly as purchased from Sigma-Aldrich with a purity of ≥99.9%. Both ends of the carbonized substrate were fixed on two copper foils by silver paste to gain good electrical contact. Then the carbon substrate was uniformly covered with the metal salt precursor solution by gradually dropping a total of 150 µL of the mixture onto it, followed by drying at 60 °C in an oven overnight. A direct electric pulse from a Keithley 2425 SourceMeter was applied to the carbon support in air. Generally, a high current pulse (3 A, 500 ms) was used. After cooling down to room temperature, the carbon support was cut from the copper electrodes for electrocatalytic testing and other characterization. HPNP with a different metal ion ratio (12.5:12.5:25:25:25) was synthesized using the same method. Control catalysts ($FeCoNiO_x$@Ir, $FeCoNiO_x$@Pt, $FeCoNiO_x$, Ir, and Pt) were fabricated using the same method but with different precursor solutions. Specifically, all precursor solutions were 0.05 mol L^{-1} and the metal ion ratio in the precursor solution for the synthesis of $FeCoNiO_x$@Ir, $FeCoNiO_x$@Pt and $FeCoNiO_x$ was 30:30:30:10, 30:30:30:10, and 1:1:1, respectively.

Electrocatalysis Measurements: The electrochemistry testing was carried out on a three-electrode setup connected to an electrochemical workstation (VMP3/Z bio-logic system). An Ag/AgCl electrode and graphite rod served as the reference and counter electrode, respectively. Freshly prepared 1 м KOH was used as electrolyte for the ORR and OER measurements. The carbon support with nanocatalysts was used as the free-standing working electrode without binder.

For OER testing, the activation process was conducted from –0.2 to 0.5 V. LSV curves were recorded from 0 to 1.0 V versus the Ag/AgCl electrode at a scanning rate of 1 mV s^{-1}. Chronoamperometry at 10 mA cm^{-2} was applied to test the stability of the catalyst. Accelerated CVs of 500 cycles was conducted from 0 to 0.55 V versus the Ag/AgCl electrode.

For the ORR experiments, RDE (5 mm diameter) was used for loading catalyst to exclude the influence of the non-planer carbon substrate. Generally, 6 mg catalyst supported on carbon substrate was firstly grinded and mixed with 750 µL isopropanol and 50 µL Nafion solution to make a mixed ink. Then 12 µL ink was drop-cast on the RDE surface to yield a HPNP catalyst loading of 55 µg cm^{-2}. A 40-cycle CV activation was first conducted from 0.2 to –0.2 V versus Ag/AgCl electrode at a scanning rate of 20 mV s^{-1} in Ar-saturated electrolyte. LSV curves were then recorded from 0 to –0.8 V versus Ag/AgCl electrode at a scanning rate of 1 mV s^{-1} with controlled rotating speeds of 800, 1200, 1600, 2000, and 2400 rpm in O_2-saturated electrolyte. The electron transfer number (*n*) was calculated from Koutecky–Levich plot, which follows the equation

$$j^{-1} = j_L^{-1} + j_k^{-1} = B^{-1} * \omega^{-0.5} + j_k^{-1} \tag{1}$$

where $B = 0.201 nFC_0 D_0^{2/3} \upsilon^{-1/6}$, *n* is the electron number related to O_2 reduction, *j* is the measured overall current density, *j* is the kinetically limited current density, *ω* is the rotating speed in unit of rpm, *F* is the Faraday constant of 96 485 C, C_0 and D_0 is the O_2 concentration and diffusion coefficient in electrolyte (1.2×10^{-6} mol cm^{-3}, 1.9×10^{-5} cm^2 s^{-1}), respectively. *ν* is the viscosity of electrolyte (10^{-2} cm^2 s^{-1}).

The method of double layer capacitance was used to evaluate the ECSA, which follows the equation of $A = C_{dl}/C_{ideal}$, where C_{ideal} is the ideal catalyst double-layer capacitance and C_{dl} is the double-layer capacitance of measured catalyst. For measurement of the double layer capacitance, CV cycles under varied scanning rates of 1, 2, 5, 10, 20, and 50 mV s^{-1} were captured from 0 to –0.1 V versus the Ag/AgCl electrode with a rotating speed of 1600 rpm. Based on the equation of $i_c = C_{dl} \times \nu$, where ν is the scanning rate and i_c is the current density, C_{dl} could be obtained from the slope of $i_c \approx \nu$ curve.

After 3000 cycles of accelerated CV from 0 to –0.4 V versus the Ag/AgCl electrode with a scanning rate of 50 mV s^{-1}, the LSV curve was captured to evaluate the stability of the catalyst.

All potentials were compensated by 85% *i*R to correct for the Ohmic drop of the solution, unless otherwise specified. The Ohmic resistance of 1 м KOH was about 6.7 Ω, which was obtained from electrochemical impedance spectroscopy (EIS) with frequency from 100 kHz to 1 Hz at open circuit potential. The potential versus Ag/AgCl was converted to the reversible hydrogen electrode (RHE), calculated from the following equation

$$E_{\text{vs RHE}} = E_{\text{vs Ag/AgCl}} + E^0_{\text{Ag/AgCl vs RHE}} + 0.059\,\text{pH} \tag{2}$$

in which $E^0_{\text{Ag/AgCl versus RHE}}$ is 0.199 V at 25 °C.

Density Functional Theory (DFT) Calculation: All the spin-polarized density functional theory (DFT) calculations were performed using Vienna Ab initio Simulation Package (VASP).[51] The projector-augmented wave (PAW) method[52] and Perdew-Burke-Ernzerhof (PBE)[53] functional was used. The Kohn–Sham wave functions were expanded in a plane wave basis set with a cutoff energy of 400 eV. The Brillouin zone was sampled by the 3 × 3 × 1 Monkhorst–Pack k-point mesh. All atoms were allowed to relax until the forces fell below 0.03 eV $Å^{-1}$. To compare the electrochemical catalysis of $FeCoNiO_4$ and the $FeCoNiO_4$ with IrPt nanoparticle, two atomic structures (56-atom $FeCoNiO_4$ atomic structure and a 56-atom of $FeCoNiO_4$ atomic structure with a 6-atom IrPt nanoparticle on it) were built. A vacuum region of 16 Å was created to ensure negligible interaction between mirror images.

The OER occurs via the following steps

$$\text{M} + \text{H}_2\text{O}_{(l)} \rightarrow \text{MOH} + \text{H}^+ + \text{e}^- \tag{3}$$

$$\text{MOH} \rightarrow \text{MO} + \text{H}^+ + \text{e}^- \tag{4}$$

$$\text{MO} + \text{H}_2\text{O}_{(l)} \rightarrow \text{MOOH} + \text{H}^+ + \text{e}^- \tag{5}$$

$$\text{MOOH} \rightarrow \text{M} + \text{O}_{2(g)} + \text{H}^+ + \text{e}^- \tag{6}$$

The ORR occurs via the following steps

$$\text{M} + \text{O}_{2(g)} + \text{H}^+ + \text{e}^- \rightarrow \text{MOOH} \tag{7}$$

$$\text{MOOH} + \text{H}^+ + \text{e}^- \rightarrow \text{MO} + \text{H}_2\text{O} \tag{8}$$

$$\text{MO} + \text{H}^+ + \text{e}^- \rightarrow \text{MOH} \tag{9}$$

$$\text{MOH} + \text{H}^+ + \text{e}^- \rightarrow \text{M} + \text{H}_2\text{O} \tag{10}$$

where *M* represents the preferable adsorption site for intermediates. For each step, the reaction free energy Δ*G* is defined as the difference between free energies of the initial and final states as calculated by the expression[54]

$$\Delta G = \Delta E + \Delta \text{ZPE} - T\Delta S + \Delta G_{\text{U}} + \Delta G_{\text{pH}} \tag{11}$$

where Δ*E* is the total energy difference between reactants and products of reactions, ΔZPE is the zero-point energy correction, Δ*S* is the vibrational entropy change at finite temperature *T*, $\Delta G_{\text{U}} = -eU$, where *e* is the elementary charge, *U* is the electrode potential, ΔG_{pH} is the correction of the H^+ free energy.

Characterization: SEM was conducted at 10 kV on a Hitachi SU-70 with EDS analysis at 15 kV. Temperature measurement of the carbonized wood during the thermal shock was estimated according to black-body radiation using a high-speed camera (Vision Research Phantom Miro M110) with a video recording speed of 3000 frames per second.[26] STEM-EDX elemental maps were acquired with a Thermo-Fisher Talos F200X. High-resolution HAADF-STEM images were obtained using a Hitachi HD2700C equipped with a probe aberration corrector and cold field-emission gun. XPS was performed on a Thermo ESCALAB 250. XRD analysis was conducted on a Bruker C2 Discover X-ray powder diffractometer. Raman spectroscopy was captured on a Jobin Yvon LabRam ARAMIS system with a laser wavelength of 532 nm. Thermogravimetric analysis (TGA) for measurement of catalyst mass loading was performed on a Discovery SDT 650 thermal analyzer by TA Instruments. The size distribution of the nanoparticles was analyzed by ImageJ.

Supporting Information

Supporting Information is available from the Wiley Online Library or from the author.

Acknowledgements

This project is supported by the National Science Foundation Scalable Nanomanufacturing Project No. 1635221. The authors acknowledge the support of the Maryland Nanocenter, and its Surface Analysis Center and AIMLab. This research used resources of the Center for Functional Nanomaterials, which is a U.S. DOE Office of Science Facility, at Brookhaven National Laboratory under Contract No. DE-SC0012704. The authors acknowledge the University of Maryland supercomputing resources (http://hpcc.umd.edu) made available for conducting the research reported in this paper.

Conflict of Interest

The authors declare no conflict of interest.

Author Contributions

M.W., M.C., and L.W. contributed equally to this work. L.H., M.W., and C.Y. conceived the idea and designed the experiments. M.W., M.C., and Q.X. carried out the synthesis of nanocatalysts. M.W., M.C., and C.Y. conducted the electrochemistry measurement. L.W. and T.L. conducted the DFT simulation and analysis. S.H. performed the STEM measurement. M.W. and Q.X. created the 3D illustrations. H.Q. and G.Z. did the characterization of Raman and TGA. X.W., D.K., and M.R.Z. contributed to the measurement of the temperature profile for the high-temperature pulse. M.C. and W.G. synthesized the activated carbonized wood. L.H., M.W., and C.Y. wrote the paper. All authors commented on the final manuscript.

Keywords

bifunctional, bifunctional electrocatalysts, electrocatalysts, hierarchical nanoparticles, oxygen electrodes, polyelemental nanoparticles

Received: March 29, 2020

[1] F. Cheng, J. Chen, *Chem. Soc. Rev.* **2012**, *41*, 2172.
[2] M. Gong, W. Zhou, M.-C. Tsai, J. Zhou, M. Guan, M.-C. Lin, B. Zhang, Y. Hu, D.-Y. Wang, J. Yang, S. J. Pennycook, B.-J. Hwang, H. Dai, *Nat. Commun.* **2014**, *5*, 4695.
[3] F. Yu, H. Zhou, Y. Huang, J. Sun, F. Qin, J. Bao, W. A. Goddard 3rd, S. Chen, Z. Ren, *Nat. Commun.* **2018**, *9*, 2551.
[4] C. C. L. McCrory, S. Jung, I. M. Ferrer, S. M. Chatman, J. C. Peters, T. F. Jaramillo, *J. Am. Chem. Soc.* **2015**, *137*, 4347.
[5] R. Bashyam, P. Zelenay, *Nature* **2006**, *443*, 63.
[6] W. Luc, M. Jouny, J. Rosen, F. Jiao, *Energy Environ. Sci.* **2018**, *11*, 2928.
[7] N.-T. Suen, S.-F. Hung, Q. Quan, N. Zhang, Y.-J. Xu, H. M. Chen, *Chem. Soc. Rev.* **2017**, *46*, 337.
[8] S. Guo, S. Zhang, S. Sun, *Angew. Chem., Int. Ed.* **2013**, *52*, 8526.
[9] X. F. Lu, Y. Chen, S. Wang, S. Gao, X. W. Lou, *Adv. Mater.* **2019**, *31*, 1902339.
[10] D.-Y. Kuo, H. Paik, J. Kloppenburg, B. Faeth, K. M. Shen, D. G. Schlom, G. Hautier, J. Suntivich, *J. Am. Chem. Soc.* **2018**, *140*, 17597.
[11] T. Reier, M. Oezaslan, P. Strasser, *ACS Catal.* **2012**, *2*, 1765.
[12] S. Cherevko, S. Geiger, O. Kasian, N. Kulyk, J.-P. Grote, A. Savan, B. R. Shrestha, S. Merzlikin, B. Breitbach, A. Ludwig, K. J. J. Mayrhofer, *Catal. Today* **2016**, *262*, 170.
[13] J. Shan, T. Ling, K. Davey, Y. Zheng, S.-Z. Qiao, *Adv. Mater.* **2019**, *31*, 1900510.
[14] B. Qiao, A. Wang, X. Yang, L. F. Allard, Z. Jiang, Y. Cui, J. Liu, J. Li, T. Zhang, *Nat. Chem.* **2011**, *3*, 634.
[15] T. Zhang, S.-C. Li, W. Zhu, Z.-P. Zhang, J. Gu, Y.-W. Zhang, *Nanoscale* **2017**, *9*, 1154.
[16] S. T. Hunt, Y. Román-Leshkov, *Acc. Chem. Res.* **2018**, *51*, 1054.
[17] P. Strasser, *Acc. Chem. Res.* **2016**, *49*, 2658.
[18] M. Cargnello, J. J. D. Jaén, J. C. H. Garrido, K. Bakhmutsky, T. Montini, J. J. C. Gámez, R. J. Gorte, P. Fornasiero, *Science* **2012**, *337*, 713.
[19] Z. Weng, W. Liu, L.-C. Yin, R. Fang, M. Li, E. I. Altman, Q. Fan, F. Li, H.-M. Cheng, H. Wang, *Nano Lett.* **2015**, *15*, 7704.
[20] J. Zhu, Z. Chen, M. Xie, Z. Lyu, M. Chi, M. Mavrikakis, W. Jin, Y. Xia, *Angew. Chem., Int. Ed.* **2019**, *58*, 7244.
[21] L. Bu, N. Zhang, S. Guo, X. Zhang, J. Li, J. Yao, T. Wu, G. Lu, J.-Y. Ma, D. Su, X. Huang, *Science* **2016**, *354*, 1410.
[22] T. Löffler, A. Savan, A. Garzón-Manjón, M. Meischein, C. Scheu, A. Ludwig, W. Schuhmann, *ACS Energy Lett.* **2019**, *4*, 1206.
[23] J. Sun, N. Guo, Z. Shao, K. Huang, Y. Li, F. He, Q. Wang, *Adv. Energy Mater.* **2018**, *8*, 1800980.
[24] S. G. Kwon, G. Krylova, P. J. Phillips, R. F. Klie, S. Chattopadhyay, T. Shibata, E. E. Bunel, Y. Liu, V. B. Prakapenka, B. Lee, E. V. Shevchenko, *Nat. Mater.* **2015**, *14*, 215.
[25] H. Yang, S. J. Bradley, X. Wu, A. Chan, G. I. N. Waterhouse, T. Nann, J. Zhang, P. E. Kruger, S. Ma, S. G. Telfer, *ACS Nano* **2018**, *12*, 4594.
[26] Y. Yao, Z. Huang, P. Xie, S. D. Lacey, R. J. Jacob, H. Xie, F. Chen, A. Nie, T. Pu, M. Rehwoldt, D. Yu, M. R. Zachariah, C. Wang, R. Shahbazian-Yassar, J. Li, L. Hu, *Science* **2018**, *359*, 1489.
[27] M. W. Glasscott, A. D. Pendergast, S. Goines, A. R. Bishop, A. T. Hoang, C. Renault, J. E. Dick, *Nat. Commun.* **2019**, *10*, 2650.
[28] H. Cheng, Z. Cao, Z. Chen, M. Zhao, M. Xie, Z. Lyu, Z. Zhu, M. Chi, Y. Xia, *Nano Lett.* **2019**, *19*, 4997.
[29] C. Ray, T. Pal, *J. Mater. Chem. A* **2017**, *5*, 9465.
[30] X. Liu, J. Iocozzia, Y. Wang, X. Cui, Y. Chen, S. Zhao, Z. Li, Z. Lin, *Energy Environ. Sci.* **2017**, *10*, 402.
[31] A. Lamberti, A. Virga, A. Chiadò, A. Chiodoni, K. Bejtka, P. Rivolo, F. Giorgis, *J. Mater. Chem. C* **2015**, *3*, 6868.
[32] Y. Yao, K. K. Fu, C. Yan, J. Dai, Y. Chen, Y. Wang, B. Zhang, E. Hitz, L. Hu, *ACS Nano* **2016**, *10*, 5272.
[33] M.-H. Tsai, J.-W. Yeh, *Mater. Res. Lett.* **2014**, *2*, 107.

[34] https://www.doitpoms.ac.uk/tlplib/ellingham_diagrams/interactive.php (accessed: May 2020).

[35] D. L. A. de Faria, S. Venâncio Silva, M. T. de Oliveira, *J. Raman Spectrosc.* **1997**, *28*, 873.

[36] A. V. Ravindra, B. C. Behera, P. Padhan, O. I. Lebedev, W. Prellier, *J. Appl. Phys.* **2014**, *116*, 033912.

[37] M. M. Shahid, P. Rameshkumar, A. Pandikumar, H. N. Lim, Y. H. Ng, N. M. Huang, *J. Mater. Chem. A* **2015**, *3*, 14458.

[38] Z. Qiu, D. He, Y. Wang, X. Zhao, W. Zhao, H. Wu, *RSC Adv.* **2017**, *7*, 7843.

[39] C. Yuan, H. B. Wu, Y. Xie, X. W. Lou, *Angew. Chem., Int. Ed.* **2014**, *53*, 1488.

[40] W. Liu, J. Bao, L. Xu, M. Guan, Z. Wang, J. Qiu, Y. Huang, J. Xia, Y. Lei, H. Li, *Appl. Surf. Sci.* **2019**, *478*, 552.

[41] M. Li, Y. P. Xiong, X. T. Liu, X. J. Bo, Y. F. Zhang, C. Han, L. P. Guo, *Nanoscale* **2015**, *7*, 8920.

[42] M. A. Sayeed, A. P. O'Mullane, *RSC Adv.* **2017**, *7*, 43083.

[43] L. Bai, X. Wen, J. Guan, *Mater. Today Energy* **2019**, *12*, 311.

[44] H.-S. Oh, H. N. Nong, T. Reier, M. Gliech, P. Strasser, *Chem. Sci.* **2015**, *6*, 3321.

[45] F. Bizzotto, J. Quinson, A. Zana, J. J. K. Kirkensgaard, A. Dworzak, M. Oezaslan, M. Arenz, *Catal. Sci. Technol.* **2019**, *9*, 6345.

[46] F. Song, L. Bai, A. Moysiadou, S. Lee, C. Hu, L. Liardet, X. Hu, *J. Am. Chem. Soc.* **2018**, *140*, 7748.

[47] J. Yi, W. H. Lee, C. H. Choi, Y. Lee, K. S. Park, B. K. Min, Y. J. Hwang, H.-S. Oh, *Electrochem. Commun.* **2019**, *104*, 106469.

[48] L. Wei, H. E. Karahan, S. L. Zhai, H. W. Liu, X. C. Chen, Z. Zhou, Y. J. Lei, Z. W. Liu, Y. Chen, *Adv. Mater.* **2017**, *29*, 1701410.

[49] Y. Y. Liang, Y. G. Li, H. L. Wang, J. G. Zhou, J. Wang, T. Regier, H. J. Dai, *Nat. Mater.* **2011**, *10*, 780.

[50] S. Xu, Y. Kim, D. Higgins, M. Yusuf, T. F. Jaramillo, F. B. Prinz, *Electrochim. Acta* **2017**, *255*, 99.

[51] G. Kresse, J. Hafner, *Phys. Rev. B* **1993**, *47*, 558.

[52] P. E. Blöchl, *Phys. Rev. B* **1994**, *50*, 17953.

[53] J. P. Perdew, K. Burke, M. Ernzerhof, *Phys. Rev. Lett.* **1996**, *77*, 3865.

[54] S. Zuluaga, S. Stolbov, *J. Chem. Phys.* **2011**, *135*, 134702.

ADVANCED
ENERGY
MATERIALS

Supporting Information

for *Adv. Energy Mater.,* DOI: 10.1002/aenm.202001119

Hierarchical Polyelemental Nanoparticles as Bifunctional Catalysts for Oxygen Evolution and Reduction Reactions

Meiling Wu, Mingjin Cui, Lianping Wu, Sooyeon Hwang, Chunpeng Yang, Qinqin Xia, Geng Zhong, Haiyu Qiao, Wentao Gan, Xizheng Wang, Dylan Kline, Michael R. Zachariah, Dong Su, Teng Li, and Liangbing Hu**

Supporting Information

Hierarchical Polyelemental Nanoparticles as Bifunctional Catalysts for Oxygen Evolution and Reduction Reactions

Meiling Wu[1], Mingjin Cui[1], Lianping Wu[1], Sooyeon Hwang, Chunpeng Yang, Qinqin Xia, Geng Zhong, Haiyu Qiao, Wentao Gan, Xizheng Wang, Dylan Kline, Michael R. Zachariah, Dong Su, Teng Li, Liangbing Hu**

[1] These authors contributed equally to this work.

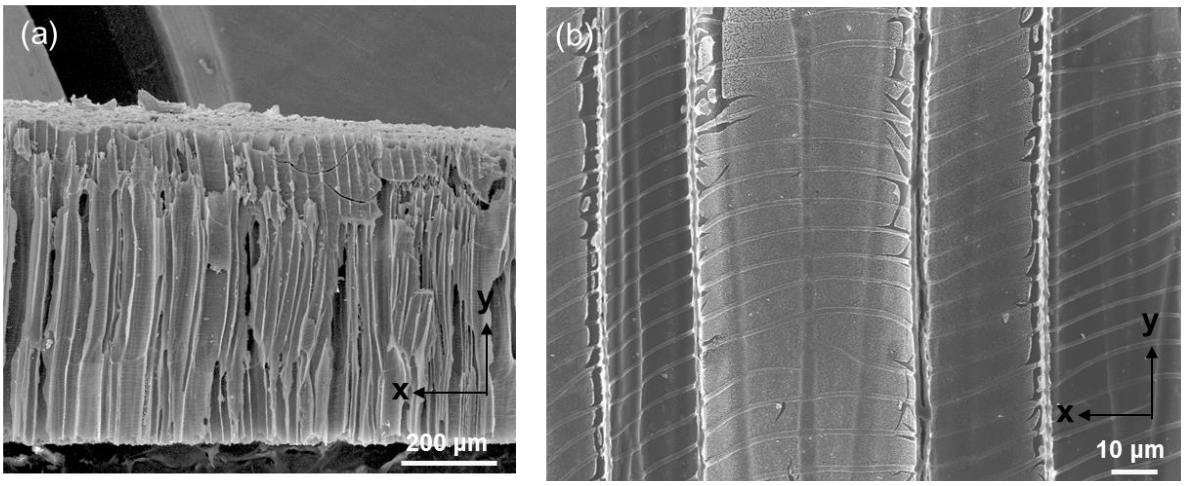

Figure S1. Cross-sectional SEM images of the carbonized wood substrate at (a) low and (b) high magnification. The porous channels along y-axis are vessel lumen of wood.

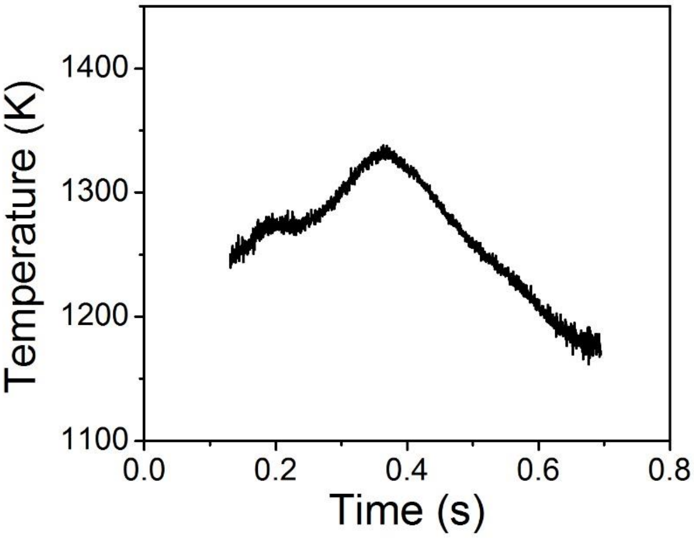

Figure S2. Temperature profile during the nanoparticle synthesis by the high-temperature pulse, which is ~1200 K for 0.5 s.

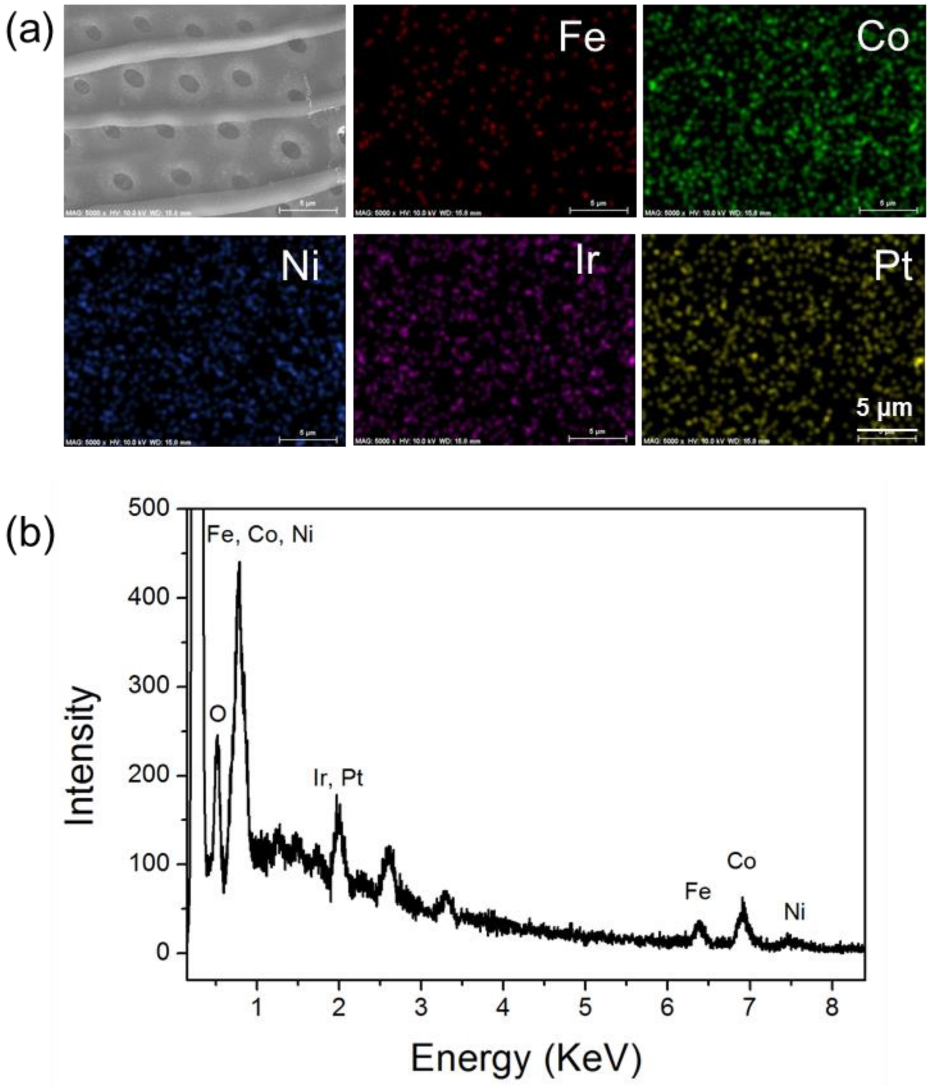

Figure S3. SEM-EDS and its corresponding mapping of polyelemental nanoparticles on the carbonized wood substrate. The uniform distribution of elements indicates the formation of polyelemental nanoparticles over a large area.

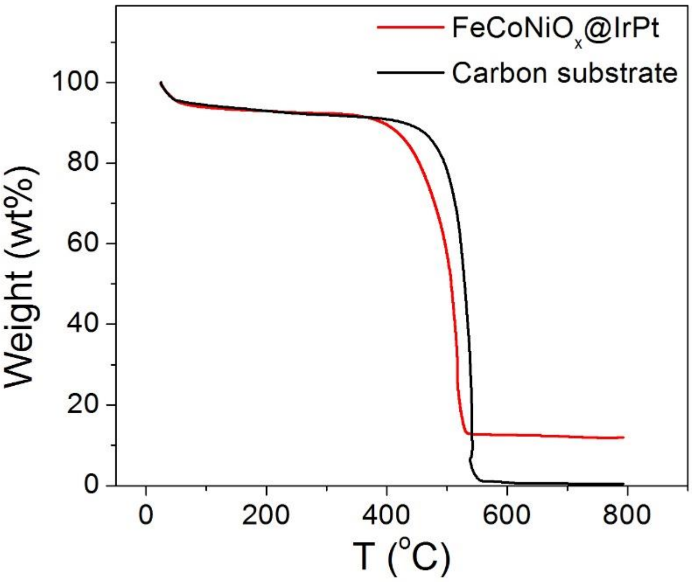

Figure S4. Thermogravimetric analysis of the nanoparticles on carbon substrate (red line) and carbon substrate (black line). The mass content of the nanoparticles was 12.0 wt%.

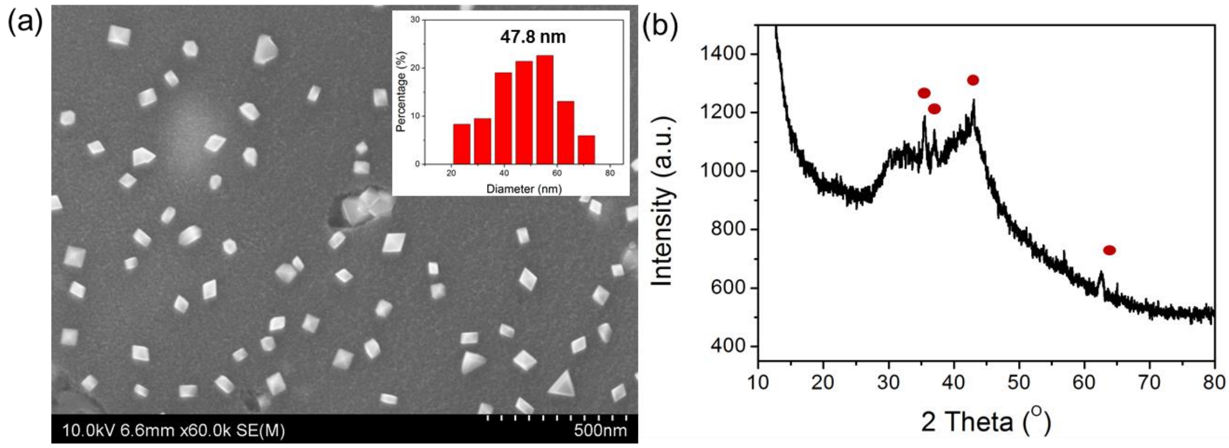

Figure S5. (a) SEM image of FeCoNiO$_x$ nanoparticles on the carbon substrate synthesized by the same high-temperature pulse method. Inset: the size distribution of the FeCoNiO$_x$ nanoparticles. (b) The XRD pattern of the FeCoNiO$_x$ nanoparticles, with characteristic peaks of spinel-structure transition metal oxides indicated.

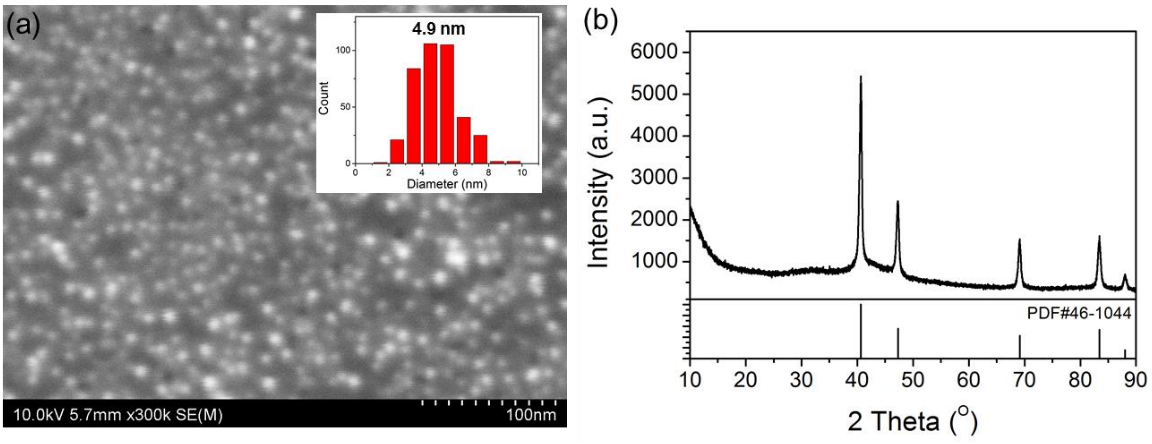

Figure S6. (a) SEM image of Ir nanoparticles on the carbon substrate synthesized by the same high-temperature pulse method. Inset: the size distribution of the Ir nanoparticles. (b) The XRD pattern of the Ir nanoparticles in consistent with the standard pattern of Ir.

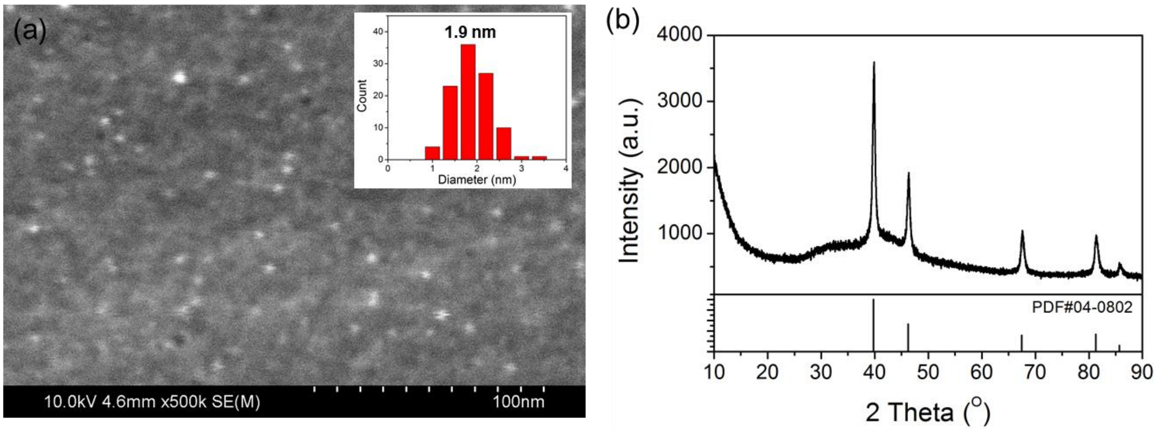

Figure S7. (a) SEM image of Pt nanoparticles on the carbon substrate synthesized by the same high-temperature pulse method. Inset: the size distribution of the Pt nanoparticles. (b) The XRD pattern of the Ir nanoparticles is consistent with the standard pattern of Pt.

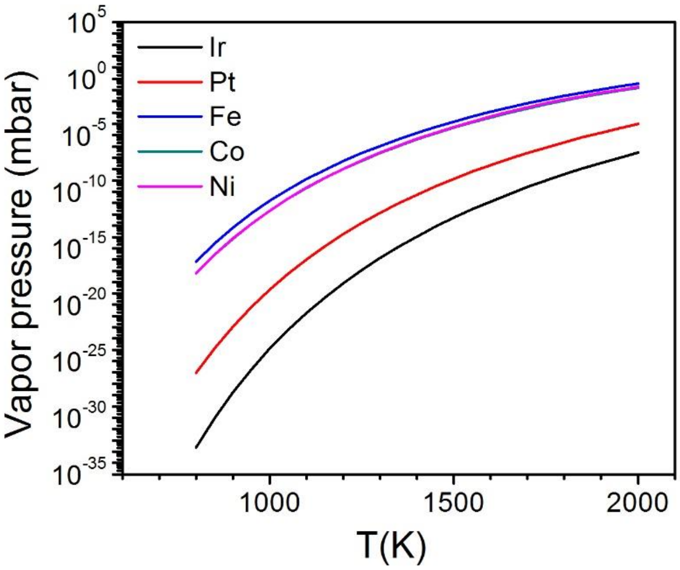

Figure S8. Vapor pressure of the different metals as a function of temperature. Data calculated from Ref [1]. The larger vapor pressure of Fe, Co, and Ni compared with Ir and Pt indicates the slower deposition rate of the transition metal vapor during the cooling process (Note that vapor pressure of Co is overlapped by that of Ni).

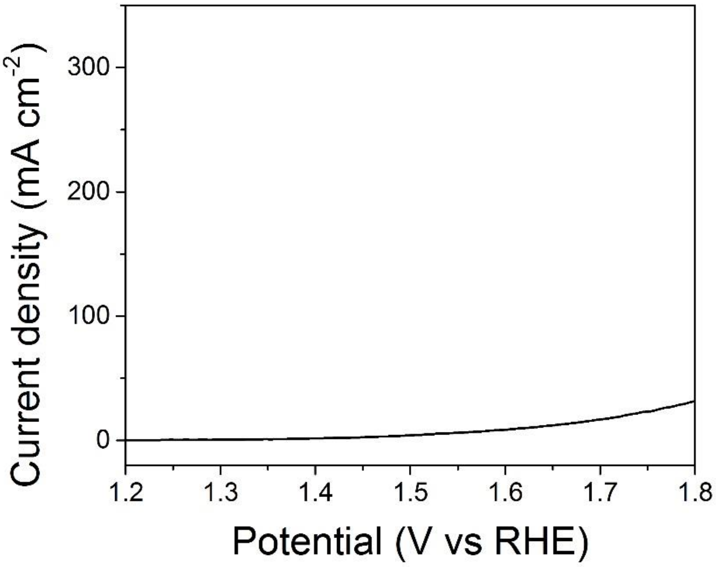

Figure S9. LSV curve of the carbon substrate by itself as a catalyst for OER. The extremely low current density of the carbonized wood at 1.6 V indicates the substrate has no catalytic activity toward OER.

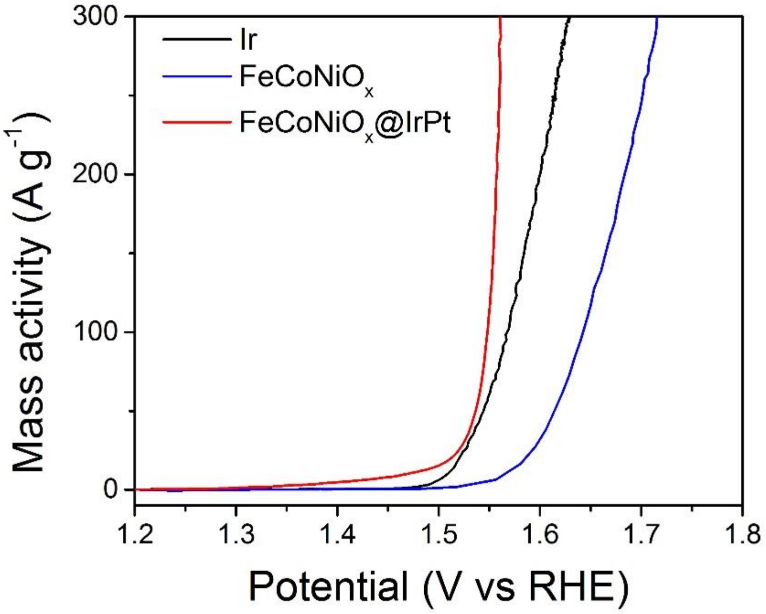

Figure S10. Mass activity of different catalysts as a function of potential, among which the polyelemental $FeCoNiO_x$@IrPt shows the best OER catalytic activity.

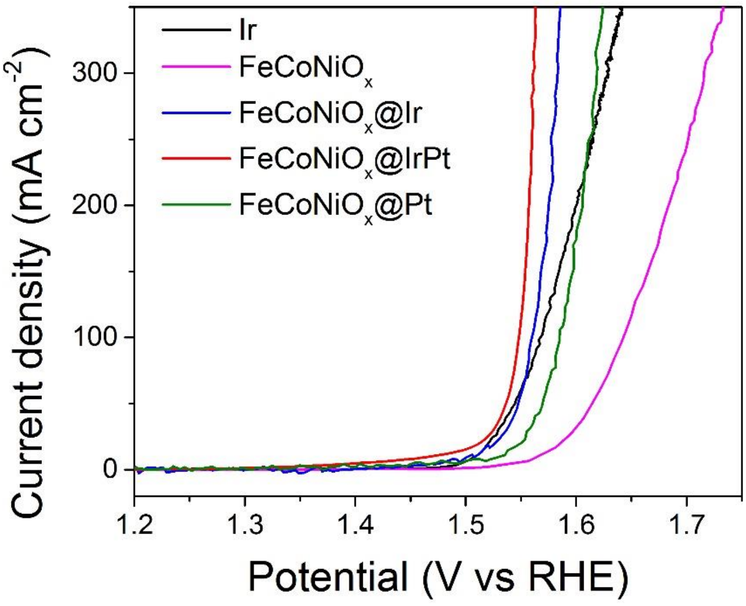

Figure S11. LSV curves of different catalysts. The potential of different catalysts for OER at current density of 10 mA cm^{-2} are: Ir, 1.51 V; $FeCoNiO_x$, 1.55 V; $FeCoNiO_x$@Pt, 1.53 V; $FeCoNiO_x$@Ir, 1.51 V; $FeCoNiO_x$@IrPt, 1.47 V (all vs. RHE).

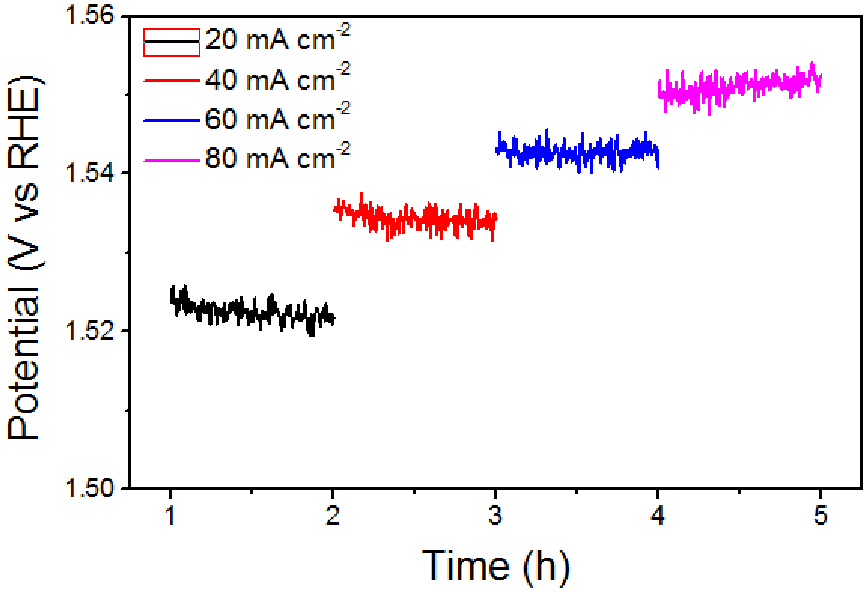

Figure S12. OER chronoamperometry of $FeCoNiO_x$@IrPt at various current densities. A stable OER performance can be obtained at high current densities up to 80 mA cm^{-2}.

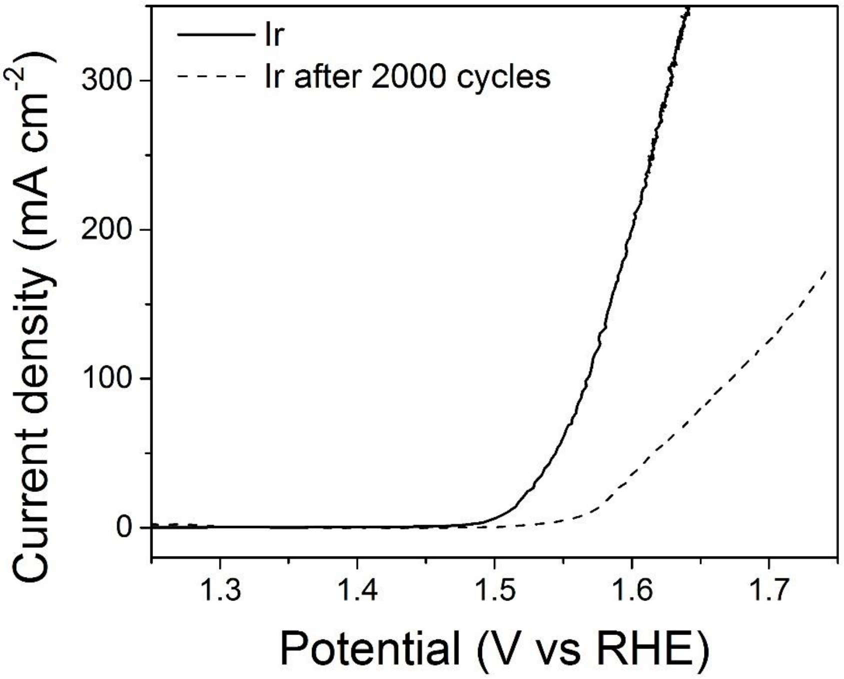

Figure S13. LSV curves of Ir before and after OER measurement. The catalytic activity of Ir degenerated significantly, in contrast the stable catalytic performance of $FeCoNiO_x$@IrPt (Figure 4d).

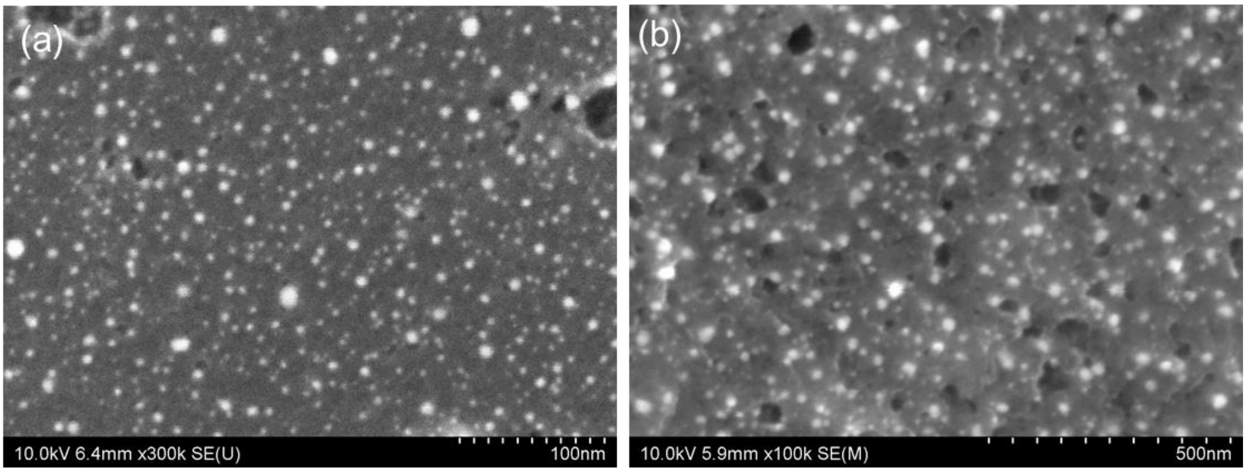

Figure S14. SEM images of FeCoNiO$_x$@IrPt (a) before and (b) after OER stability testing for 50 h at a current density of 10 mA cm^{-2}. The nanoparticles retain their uniform distribution and similar size, with no evidence of agglomeration.

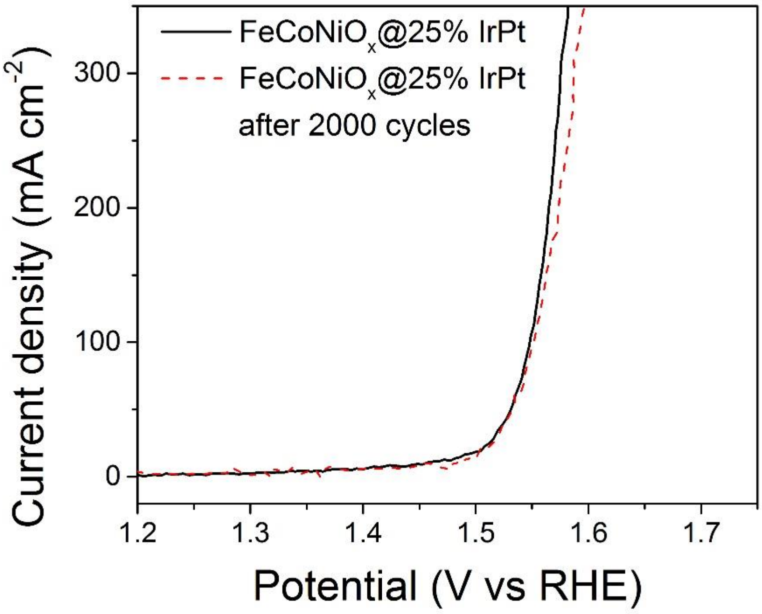

Figure S15. LSV curves of FeCoNiO$_x$@25%IrPt before and after CV measurement for 2000 cycles. The OER overpotential of FeCoNiO$_x$@25%IrPt HPNP increased slightly to 250 mV at 10 mA cm^{-2} (comparing to 240 mV of FeCoNiO$_x$@10%IrPt). The FeCoNiO$_x$@25%IrPt nanocatalyst also exhibits excellent stability for 2000 cycles, indicating the structural stability advantage of the polyelemental nanocatalyst.

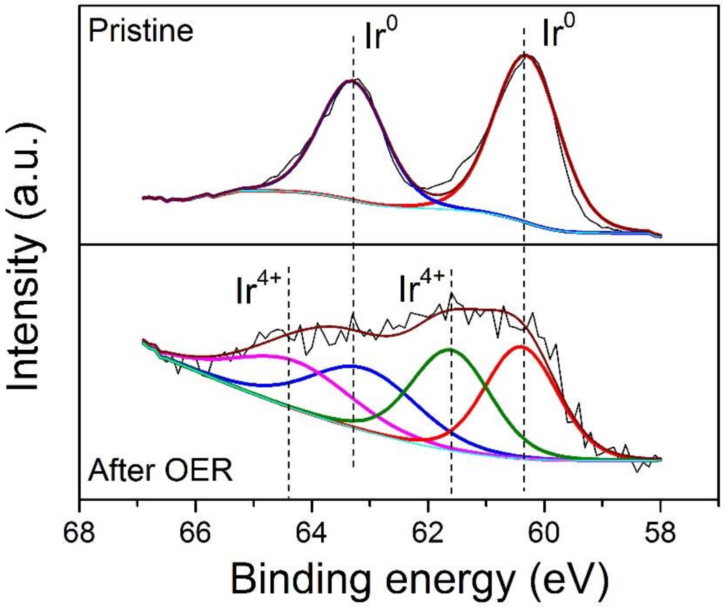

Figure S16. Ir XPS spectra of FeCoNiO$_x$@IrPt before and after stability test (accelerated CV measurements). The Ir was oxidized to IrO$_x$ on the surface of the FeCoNiO$_x$@IrPt HPNPs, which is the active site for OER in consistence with the previous literature.

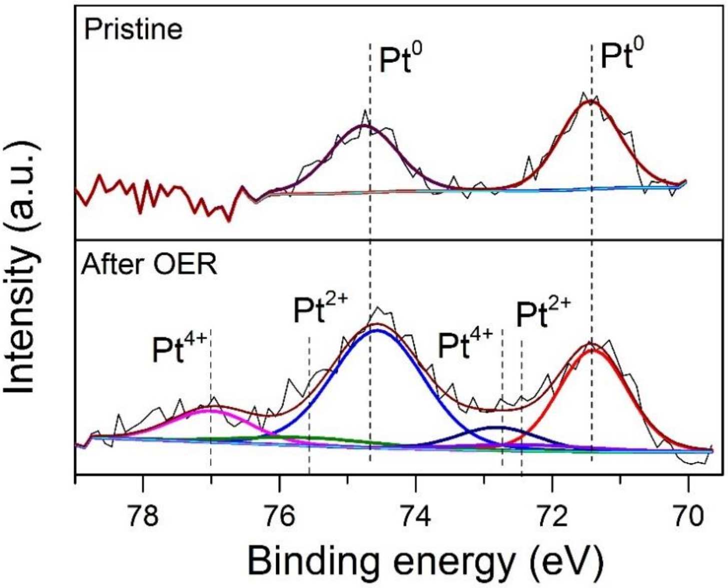

Figure S17. Pt XPS spectra of FeCoNiO$_x$@IrPt before and after stability test (accelerated CV measurements). Pt was oxidized to high valences after OER under high potential to form mixed IrPtO$_x$, further decreasing the dissolution of Ir into the alkaline solution.

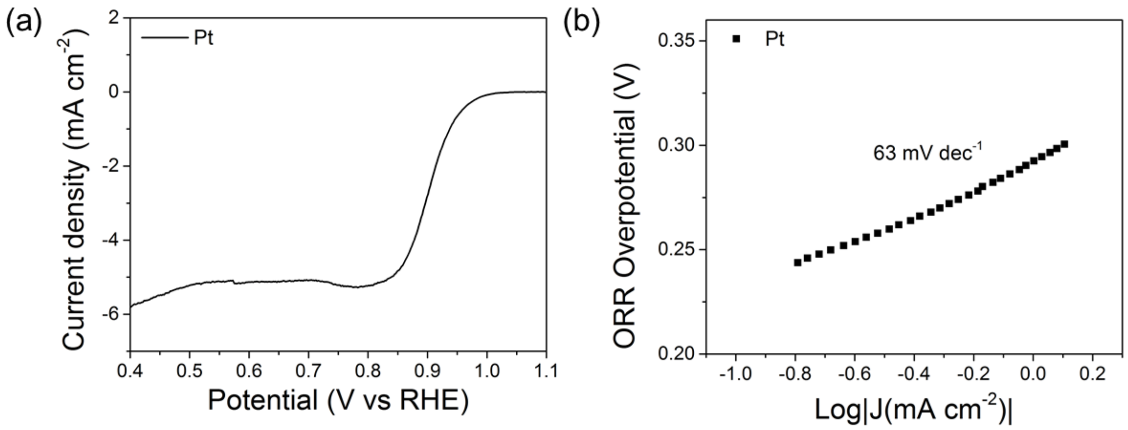

Figure S18. LSV curve and Tafel plot of the Pt nanoparticles for ORR.

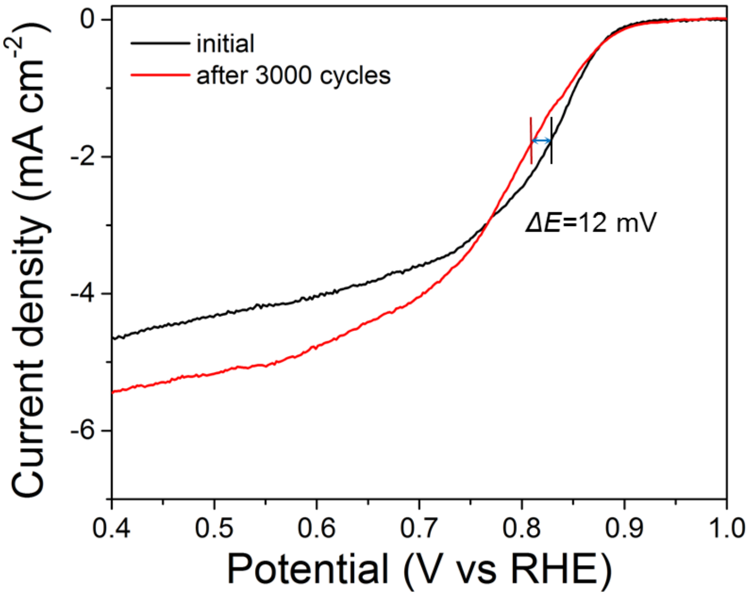

Figure S19. The first and 3000th LSV curves of FeCoNiO$_x$@IrPt in ORR by accelerated CV at 50 mV s^{-1} for 3000 cycles. The $E_{1/2}$ of the FeCoNiO$_x$@IrPt catalyst only shifted by ~12 mV after 3000 cycles, demonstrating the stability of FeCoNiO$_x$@IrPt over long-term ORR.

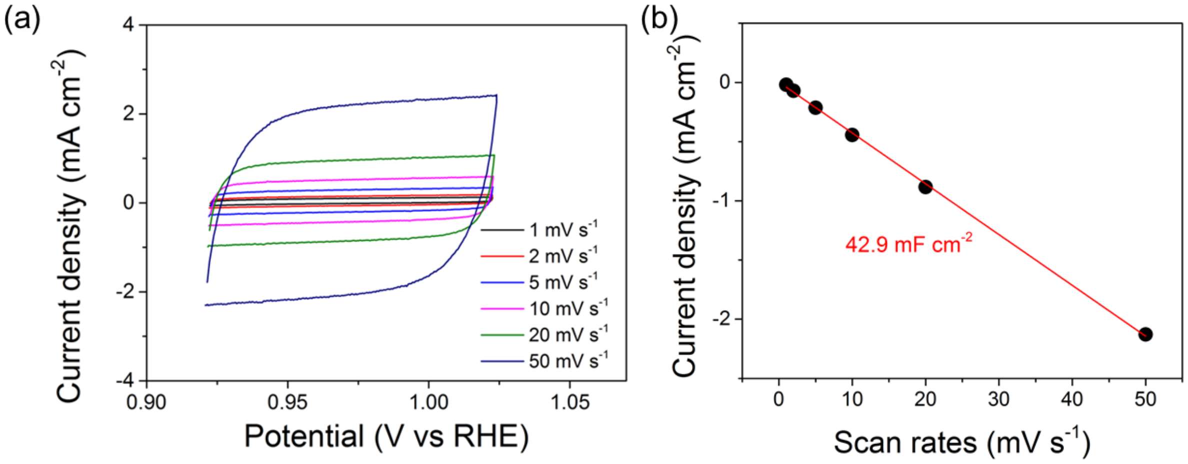

Figure S20. (a) CV curves of FeCoNiO$_x$@IrPt at different scan rates. (b) Corresponding current density as function of scan rates of FeCoNiOx@IrPt for calculating the ECSA. Based on the current density at different scan rates, the FeCoNiO$_x$@IrPt hierarchical nanoparticles possess a high double layer capacitance of 42.9 mF cm^{-2}, indicating a large ECSA.

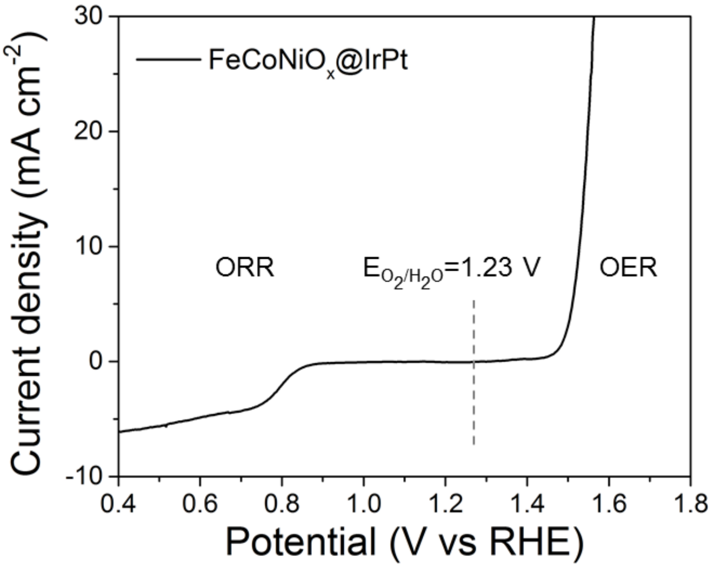

Figure S21. Full reactions of the OER/ORR performance of the FeCoNiO$_x$@IrPt nanocatalyst

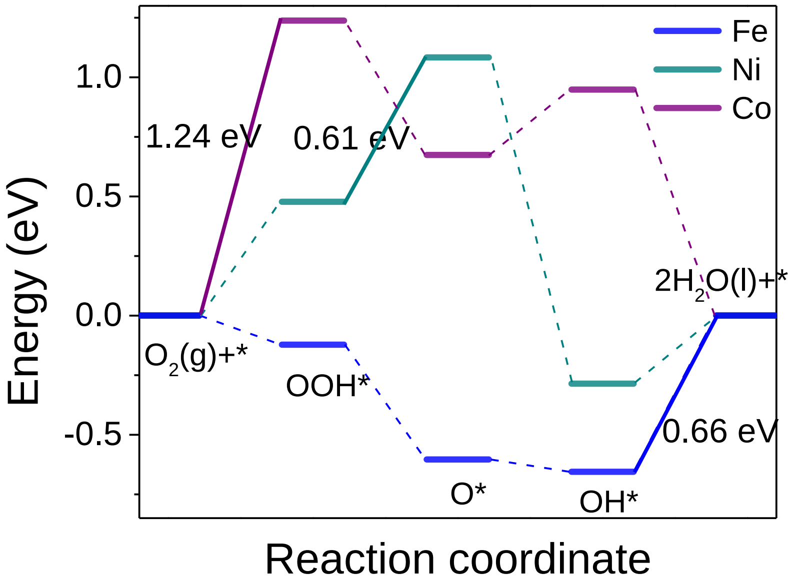

Figure S22. Free energy diagram at 1.23 V for ORR over Fe, Ni Co site on $FeNiCoO_4$ atomic structure. The highlights indicate the rate-determining step with the values of the limiting energy barrier labelled.

Table S1. OER performances of different transition metal oxide nanocatalysts.

Catalyst	Electrolyte	Mass loading [mg]	**OER OVERPOTENTIAL [V at 10 mA cm^{-2}]**	Tafel slope [mV dec^{-1}]	Ref.
FeCoNiO$_x$@IrPt	1 M KOH	0.35	240	57	This work
CoFe$_2$O$_4$	0.1 M KOH	0.03	370@5 mA cm^{-2}	82	[2]
NiFe$_2$O$_4$	0.1 M KOH	0.03	440@5 mA cm^{-2}	98	[2]
LiCoO$_2$	0.1 M KOH	0.25	320	52	[3]
MnCo oxide/N-doped CNTs	0.1 M KOH	0.21	265	-	[4]
FeCoNiO$_x$	0.1 M KOH	-	340	32	[5]
Ni$_{1.5}$Co$_{0.75}$Mn$_{0.75}$O$_4$	0.1 M KOH	0.25	540	68	[6]
FeCoNi oxide	1 M KOH	0.04	240	45	[7]
Ni$_{0.9}$Fe$_{0.1}$O$_x$	1 M KOH	1.17 µg	336	30	[8]
MnCo$_2$O$_{4.5}$	0.1 M KOH	0.28	390@20 mA cm^{-2}	144	[9]
NiFeCu	1 M KOH	10.2 ± 0.5	180	33	[10]
CoNiFe sulfide	1 M KOH	-	199	49.5	[11]
Fe$_{0.5}$Co$_{0.5}$O$_x$	1 M KOH	0.5	257	30.1	[12]

GCE: glass carbon electrode

QCM: quartz crystal microbalance

WILEY-VCH

Table S2. ORR performances of different transition metal oxide/sulfide nanocatalysts.

Catalyst	Electrolyte	Mass loading [mg cm^{-2}]	$E_{1/2}$ [V]	Tafel slope [mV dec^{-1}]	Ref.
FeCoNiO$_x$@IrPt	1 M KOH	0.35	0.83	44	This work
LiCoO$_2$	0.1 M KOH	0.25	0.68	-	[3]
MnCo oxide/N-doped CNTs	0.1 M KOH	0.21	0.82	-	[4]
Co$_3$O$_4$/N-rGO	0.1 M KOH	0.1	0.83	42	[13]
CoNiFe sulfide	0.1 M KOH	0.2	0.78	-	[11]
Fe$_{0.5}$Co$_{0.5}$O$_x$	0.1 M KOH	0.5	0.84	62.2	[12]

References

[1] M. Schmid, *Vol. 2013*, IAP/TU Wien surface physicals group.

[2] M. Li, Y. P. Xiong, X. T. Liu, X. J. Bo, Y. F. Zhang, C. Han, L. P. Guo, *Nanoscale* **2015**, *7*, 8920.

[3] T. Maiyalagan, K. A. Jarvis, S. Therese, P. J. Ferreira, A. Manthiram, *Nat. Commun.* **2014**, *5*, 2349.

[4] A. Q. Zhao, J. Masa, W. Xia, A. Maljusch, M. G. Willinger, G. Clavel, K. P. Xie, R. Schlogl, W. Schuhmann, M. Muhlert, *J. Am. Chem. Soc.* **2014**, *136*, 7551.

[5] M. Abu Sayeed, A. P. O'Mullane, *RSC Adv.* **2017**, *7*, 43083.

[6] P. Sivakumar, P. Subramanian, T. Maiyalagan, A. Gedanken, A. Schechter, *Mater. Chem. Phys.* **2019**, *229*, 190.

[7] L. Bai, X. Wen, J. Guan, *Mater. Today Energy* **2019**, *12*, 311.

[8] L. Trotochaud, J. K. Ranney, K. N. Williams, S. W. Boettcher, *J. Am. Chem. Soc.* **2012**, *134*, 17253.

[9] Z. Y. Bai, J. M. Heng, Q. Zhang, L. Yang, F. F. Chang, *Adv. Energy Mater.* **2018**, *8*, 1802390.

[10] P. L. Zhang, L. Li, D. Nordlund, H. Chen, L. Z. Fan, B. B. Zhang, X. Sheng, Q. Daniel, L. C. Sun, *Nat. Commun.* **2018**, *9*, 381.

[11] H. Z. Yang, B. Wang, H. Y. Li, B. Ni, K. Wang, Q. Zhang, X. Wang, *Adv. Energy Mater.* **2018**, *8*.

[12] L. Wei, H. E. Karahan, S. L. Zhai, H. W. Liu, X. C. Chen, Z. Zhou, Y. J. Lei, Z. W. Liu, Y. Chen, *Adv. Mater.* **2017**, *29*, 1701410.

[13] Y. Y. Liang, Y. G. Li, H. L. Wang, J. G. Zhou, J. Wang, T. Regier, H. J. Dai, *Nat. Mater.* **2011**, *10*, 780.